

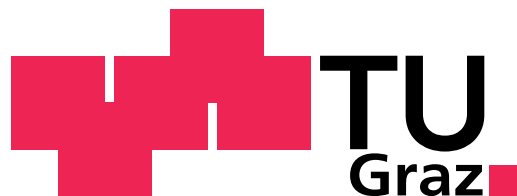
Autonomous Multi-Source Energy Harvesting System with Maximum Power Point Tracking

Masterarbeit

MA729

Marcus Dietl

Institut für Elektronik
Technische Universität Graz
Vorstand: Univ.-Prof. Dipl.-Ing. Dr. techn. Wolfgang Bösch



In Zusammenarbeit mit:
Institut für Technische Informatik
Technische Universität Graz
Vorstand: O. Univ.-Prof. Dipl.-Ing. Dr. techn. Gernot Kubin

Begutachter: Ass.-Prof. Dipl.-Ing. Dr. techn. Peter Söser
Betreuer: Dr. techn. Dipl.-Ing. BSc, Leander Bernd Hörmann

Graz, September 2013

Kurzfassung

Kürzliche Ereignisse in der Obersteiermark (St. Lorenzen, Anm.) zeigen die Wichtigkeit der Überwachung von gefährdeten Hängen zur Erkennung von Murenabgängen. Dies soll einerseits den Einsatzkräften ermöglichen sich ein schnelles Bild der Lage zu machen und gezielt eingreifen zu können, andererseits soll auch die Bevölkerung im Ernstfall alarmiert werden können um zivile Opfer zu vermeiden. In einer weiteren Arbeit könnte dieses System auch für die Erkennung von Lawinenabgängen adaptiert werden.

In einer vorhergehenden Projektarbeit wurde ein Prototyp zur Überwachung eines gefährdeten Hanges entwickelt. Für die notwendigen Messdaten wurden vom Institut für Geodäsie an der TU Graz Luftfeuchtigkeits-, Licht- und Temperaturmessung spezifiziert. Mit diesen Parametern und den GPS Daten kann eine Warnstufe für den Hang ausgegeben werden.

In dieser Masterarbeit liegt das Hauptaugenmerk auf der Entwicklung eines Energieversorgungssystems, damit der Sensorknoten autark betrieben werden kann und keine Wartungsarbeiten durchgeführt werden müssen. Als Energiequellen sollen Umgebungsenergien (Solar, Thermische Energie, etc.) in Kombination mit einem Energiespeicher (Batterie) dienen. Um Versorgungsengpässe in der Energieversorgung zu vermeiden, wird mittels der Methode der Verfolgung der maximalen Energieabgabe und der Verwendung eines Ladecontrollers das System in einen autarken Zustand versetzt.

Abstract

Recent occurrences of landslides in Upper Styria show the importance of a monitoring system in endangered areas. On the one hand this should greatly help the relief units to be able to react faster to a growing threat and on the other hand it will be possible to alarm the public and avoid casualties. Further proceedings of this work could lead to a development to monitor avalanches in inner alpine areas.

In an anterior master project, a sensor node had been developed which is capable of collecting GPS data and measuring temperature, humidity and accelerations of the prototype. These parameters had been defined by the Institute for Geodesy at Graz University of Technology as necessary to determine the risk of a landslide.

In this master thesis the main focus will be the development of a maintenance-free energy harvesting system which supplies the sensor node. A combination of alternative energies, like photovoltaic cells or thermoelectric generators, as well as energy storage devices will serve as energy sources. To maximize the power output, maximum power point tracking algorithms and a charging IC are used.

STATUTORY DECLARATION

I declare that I have authored this thesis independently, that I have not used other than the declared sources / resources, and that I have explicitly marked all material which has been quoted either literally or by content from the used sources.

Graz, August 30th 2013

.....
(signature)

Acknowledgements

Diese Diplomarbeit wurde im Zuge des Studienjahres 2012/2013 am Institut für Elektronik in Zusammenarbeit mit dem Institut für Technische Informatik an der TU Graz durchgeführt.

Diese Seite soll jenen Personen gewidmet sein, die mich bei der Erstellung dieser Arbeit unterstützt haben.

Bedanken möchte ich mich bei Christian Steger und Peter Söser, die diese Arbeit möglich gemacht haben, und immer ein offenes Ohr für meine Anliegen hatten.

Besonderer Dank geht an Leander Hörmann für die Betreuung dieser Arbeit und Friedrich Lobenstock für die interessanten fachlichen Diskussionen.

Abschließend möchte ich mich vor allem bei meinen Eltern bedanken, ohne deren Hilfe dieses Studium nicht möglich gewesen wäre.

Graz, im August 2013, Marcus Dietl

Contents

1	Introduction	1
1.1	Motivation	2
1.2	Outline	2
1.3	Organization	3
2	Related Work	5
2.1	Energy Storage and Harvesting	5
2.1.1	Primary and Secondary Energy Sources	7
2.1.2	Harvesting	9
2.2	Maximum Power Point Tracking	14
2.3	Power Converter	16
2.3.1	Buck Converter	18
2.3.2	Boost Converter	18
2.3.3	SEPIC Converter	19
2.3.4	Split-Pi Converter	19
2.3.5	Electronic Control Unit	20
2.4	Summary	20
3	Solution Approaches	21
3.1	Energy Sources	21
3.1.1	Energy Harvesting	22
3.1.2	Energy Storage	22
3.2	Hardware Design	23
3.2.1	Power Supply	23
3.2.2	Microcontroller	23
3.2.3	Reverse Current Mode	24
3.2.4	Maximum Power Point Tracking	25
3.2.5	Battery Charging	26
3.2.6	Connector	26
3.3	Software Design	27
3.3.1	Maximum PowerPoint Tracking	28
3.3.2	Activation Interval	28
3.4	Mounting	28
3.5	Summary	28

4	Implementation	31
4.1	Hardware	31
4.1.1	Energy Sources	32
4.1.2	Maximum Power Point Control	35
4.1.3	Reverse Current Mode Control	41
4.1.4	Battery Charging	45
4.1.5	Current and Voltage Measurement	48
4.1.6	Power Supply	48
4.2	Software	50
4.2.1	Interrupt Service Routines	51
4.2.2	Reverse Current Mode (RCM)	51
4.2.3	MPP Tracking Algorithms	53
4.2.4	Implementation	54
4.3	Mounting	55
4.4	Conclusion	57
5	Results	59
5.1	Energy Source	59
5.2	Reverse Current Mode	62
5.3	Maximum Power Point Tracking	64
5.3.1	Selection of an algorithm	64
6	Conclusion and Outlook	67
6.1	System Overview	67
6.2	Improvements	68
A	Acronyms and Abbreviations	69
A.1	Functional Block Diagram LTC4000-1	71
A.2	Simulation Model of the MPP Tracker	72
B	Schematics and Layout	73
	Bibliography	78

List of Figures

1.1	Relation between sensing distance and integration density in wireless sensor nodes [15]	1
1.2	Basic sensor architecture in wireless sensor networks.	2
2.1	Architecture of an energy harvesting system. Power management will be the focus of this thesis.	5
2.2	Proposed architecture for an Energy Harvesting Transducer [25]	6
2.3	Energy harvesting system design of the AmbiMax project [19]	7
2.4	Proposed energy harvesting platform Managy [24]. The possibility to supply the load from five different energy sources makes it reliable in all situations.	7
2.5	Temperature influence on position of maximum output power, BP-350U datasheet	11
2.6	Incident solar power under different weather conditions, [13]	11
2.7	Average Power output of a solar cell that is inclined under an angle α in a certain geographic direction per year, [13]	11
2.8	Power output of a solar cell inclined under an angle α [13]	11
2.9	Composition of a semiconductor TEMG, [6]	12
2.10	The operating principle of an n-type semiconductor in a thermoelectric module, [7]	12
2.11	Expected output power and open circuit voltage of a thermoelectric module, [6]	12
2.12	Electronic circuit for charging a 3V lithium battery from a TEMG input with the LTC3108 DC/DC converter, [6]	13
2.13	Possibility for using electromagnetic radiation from the environment [10]	13
2.14	Maximum Power Point Tracking at different irradiation, [1]	14
2.15	A representation of a Pilot Cell Maximum Power Point Tracking architecture, [2]	15
2.16	Representation of an adaptive system to track the MPP, [3]	16
2.17	Sequence flow of the Incremental Conductance Algorithm, [5]	17
2.18	Basic Buck Converter, [8]	18
2.19	Basic Boost Converter, [8]	18
2.20	Basic SEPIC Converter, [8]	19
2.21	Simulation of a Split-Pi converter in PSpice 8	19
3.1	The basic concept of an energy harvesting system architecture, whereas the thicker lines show the energy flow and the thinner ones the information flow.	24

3.2	Solar cell covered in snow before reverse current mode	25
3.3	Not the entire snow layer slid off, however, due to the frame	25
3.4	Voltage and current characteristics for charging a lead-acid battery [17] . .	27
4.1	Implemented Design of the Energy Harvesting System. Bolt arrows show the energy flow, whereas the thin arrows show the information flow.	32
4.2	Basic architecture of the thermoelectric generator [31]	33
4.3	Basic architecture of a TEMG with a heat box [31]	33
4.4	Measuring the temperature difference between soil and top of a heat pipe, [31]	33
4.5	Heat box. Measuring the temperature difference between the liquid and top of the heat pipe, [31]	34
4.6	Suggested design of the SEPIC converter to track the maximum power point in PowerStageDesigner	37
4.7	Voltage and maximum current characteristic at the primary coil (L1), Pow- erStageDesigner	38
4.8	Voltage and maximum current characteristic at the secondary coil (L2), PowerStageDesigner	38
4.9	Voltage and maximum current characteristic at the n-MosFET (Q1), Pow- erStageDesigner	39
4.10	Maximum voltage and current characteristic at the Schottky diode (D1), PowerStageDesigner	39
4.11	Changing the resistor value for MPP tracking in serial mode, complete schematic.	40
4.12	In case the digital potentiometer is not supplied, the JFET is turned on and a correct resistor divider is seen on the IFB pin.	40
4.13	In case the digital potentiometer is supplied, the JFET is switched off via the microcontroller and the MCP4152 gives the correct resistor size.	40
4.14	Changing the resistor value for MPP tracking in parallel mode	40
4.15	Suggested design of the reverse current mode in PowerStageDesigner	43
4.16	Voltage and maximum current characteristic at the primary coil (L1), Pow- erStageDesigner	44
4.17	Voltage and maximum current characteristic at the secondary coil (L2), PowerStageDesigner	44
4.18	Voltage and maximum current characteristic at the n-MosFET (Q1), Pow- erStageDesigner	45
4.19	Maximum voltage and current characteristic at the Schottky diode (D1), PowerStageDesigner	45
4.20	Reverse polarity protection for the lead acid battery, simulated in LTSpice.	47
4.21	Transient protection of a current-shunt monitor using a resistor in series with a zener diode	49
4.22	Design of the 3.4 V power supply to the sensor node	50
4.23	Sequence flow of the EHS programme	51
4.24	Sequence diagram of the Port Interrupt Service Routine for different cases .	52
4.25	Sequence diagram of the Reverse Current Mode (RCM)	52
4.26	Sequence diagram of the Fractional Open Circuit control algorithm	53

4.27	Sequence diagram of the Perturb and Observe algorithm	54
4.28	Overview of the connections between single processes	55
4.29	A barebone case with already drilled sensor connectors.	56
4.30	Including a GPS receiver and a sensor node mounted on plexiglass.	56
4.31	A sealed sensor node with harvesting system in case.	56
4.32	Complete system mounted on a rod with connected battery and GPS antenna. Test carried out in Wald am Schoberpass, Styria.	56
5.1	Schematic representation of a solar cell with diodes and a current source.	59
5.2	Simulation result of the used solar cell model. In the first graph one can obtain the output power whereas the second graph illustrates the U-I characteristics for a wide temperature range.	60
5.3	Output power measurement of a solar cell that had been placed on a north-facing balcony.	61
5.4	U-I characteristics of the used solar cell, located on a north-facing balcony.	61
5.5	Temperature rise of the Mosfet and the solar panel during the stress test.	63
5.6	Temperature decrease of Mosfet and solar panel after switching off the reverse current mode.	63
5.7	Simulation results for a whole charging cycle at a temperature of 50 °C.	65
A.1	Block diagram of the LTC4000-1 charging IC, [37]	71
B.1	Schematics of the Energy Harvesting System (1/3)	74
B.2	Schematics of the Energy Harvesting System (2/3)	75
B.3	Schematics of the Energy Harvesting System (3/3)	76
B.4	Layout of the Energy Harvesting System	77

List of Tables

- 2.1 Overview of most common batteries and their attributes compared to a supercapacitor. Values taken from [17][22] 9
- 2.2 Overview of most common energy harvesting sources and their potential . . 10
- 2.3 Overview of measured and calculated efficiencies of most common MPPT techniques, [4] 16

- 4.1 Comparison of the serial and parallel methods to control the MPP. V_{MPP} is the voltage of the maximum power point, $R_{ifb2,needed}$ is the needed resistor to form the correct resistor divider to the IFB pin and the resolutions are given in bits. 41

- 5.1 Measurement of the temperature on the power Mosfet and the solar panel when driving system into reverse current mode. 62
- 5.2 Measurement of the decrease in temperature on a solar panel and the power Mosfet after switching off the reverse current mode. 62

Chapter 1

Introduction

The dream of every embedded system developer would be an electronic environment in which a person can control their environment by simply being present. This smart infrastructure could be composed of embedded sensors or actuators in objects that are used for normal everyday life. As the integration of cheap but powerful and customizable devices advances, it is merely a question of time when large computers or even laptops are replaced.

Moore's law of doubling the transistor density every two to three years can also somehow be applied to wireless sensor networks. In this case, the integration density declines with increasing sensing distance which is shown in Figure 1.1. Note that increasing transmitting power to overcome sensing distance will always result in higher overall power consumption and, therefore, in a bigger design. Typically, a wireless sensor network (WSN) is made up

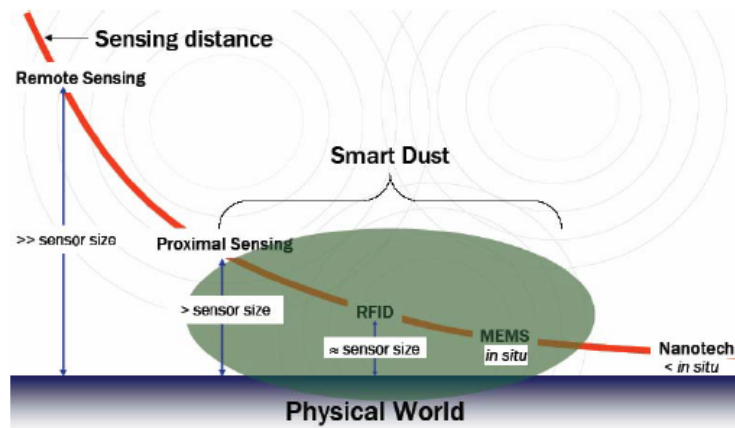


Figure 1.1: Relation between sensing distance and integration density in wireless sensor nodes [15]

of a few up to hundreds of sensor nodes that are capable of gathering environmental data and transmitting them over a bridge or directly to a base station. Environmental data can be understood as pressure, air humidity or light intensity measurements.

The basic architectures of wireless sensor nodes are illustrated in Figure 1.2. Whereas in

the early days of wireless sensor networks the sensor node was always powered by batteries, nowadays, a different approach with energy harvesting as the energy source is applied. Common power management approaches consist of switching regulators or LDOs to provide the necessary voltage levels to the Microcontroller Unit (MCU). An RF connection ensures that the measured data are transmitted to the base station respectively actuator data can be received.



Figure 1.2: Basic sensor architecture in wireless sensor networks.

1.1 Motivation

A few days of heavy rain and there is a strong possibility of landslides going down the hillside. Earlier, detection was more of a foreign word than a usual concern and so nearly every year one could read in the newspapers just how devastating the last landslide had been. Monitoring is essential for predicting the behaviour and consequences of landslides. Forecasts are even more important for saving lives and evacuating persons in the affected area in time.

In Austria, the landslide danger areas are rather well known, so an early warning and monitoring system in such an area could be of a great help.

For this purpose the FFG (Österreichische Forschungsförderungsgesellschaft) founded a consortium consisting of several partners in the industry and the Technical University of Graz. The project title is referred to as GeoWSN and its project lifespan is about two years. This Master Thesis is carried out in cooperation with the Institute for Technical Informatics and the Institute for Electronics and focuses on the hardware development.

1.2 Outline

The goal of this Master Thesis is to develop an Energy Harvesting System (EHS) that can be combined with an existing sensor node to form a self-sufficient Landslide Monitoring System.

In an anterior master project, a sensor node had been developed that is capable of determining its own exact position with a millimetre-exact certainty and transmits measured data like air temperature and humidity with a multi-hopping algorithm over a ZigBee module to a nearby base station [16].

The major focus in the hardware development is on the closed-loop control of the Maximum Power Point. This is necessary to sustain and prolong the life duration of the sensor

node in the field.

All requirements in detail that should be met with the hardware:

- Reverse current mode to melt the snow layer on the photovoltaic cell
- Efficient charging of the backup battery
- Maximum power point tracking
- Possibility of feeding the system from alternative energies like thermoelectric harvesting
- Measurement of parameters like the State of Charge (SoC) of the battery and transmission to the sensor node via I2C

1.3 Organization

This Master Thesis is divided into six chapters. Starting with chapter one, an introduction to the topic is given. In chapter two, some related work and similar projects are discussed that will show us the importance of landslide monitoring.

The concept and a fairly rough approach is given in chapter three. The following chapter, the implementation, is divided into two sections: The implementation of the hardware and the integration of the necessary software on the Microcontroller.

The final two chapters deal with the experimental results, when the Energy Harvesting Device and the Sensor Node are put together, as well as an extensive conclusion covering the basic idea and the final implementation.

Chapter 2

Related Work

This chapter deals with the different aspects of energy management in wireless sensor nodes. First, energy storage and harvesting will be discussed. There is a lot of related work on the topic of combining harvesting technologies with common batteries, and respectively, capacitors. With the use of harvesting technologies, one should be aware of the problem of maximum power point tracking, which will be the second point. Approaches to keep a system in the maximum power point are presented. The last section in this chapter focuses on power converters which are commonly used to regulate output voltages to supply the load.

2.1 Energy Storage and Harvesting

The most basic architecture of a wireless sensor node would consist of three parts:

- with or without harvesting
- Power Management: MPP Tracking, Voltage Level Regulation, ...
- Load: MCU, Radio, ...

Although harvesting is not necessarily needed, it is often used to prolong the lifetime of the sensor node.



Figure 2.1: Architecture of an energy harvesting system. Power management will be the focus of this thesis.

Prior to investigating the single components of an energy harvesting system, there are already a few projects that use different designs and implementations. [25] presents actual developments in energy harvesting systems and the role model of energy harvesting transducers. A general structure of how such an energy transducer can look like is given in Figure 2.2 and covers the most common components in wireless sensor nodes. Deploying a sensor network requires an approach for selecting the hardware and software depending on the application area. In industrial sites there would be the possibility to use vibrational energy from huge rotating equipment like motors. One of the first multi-source

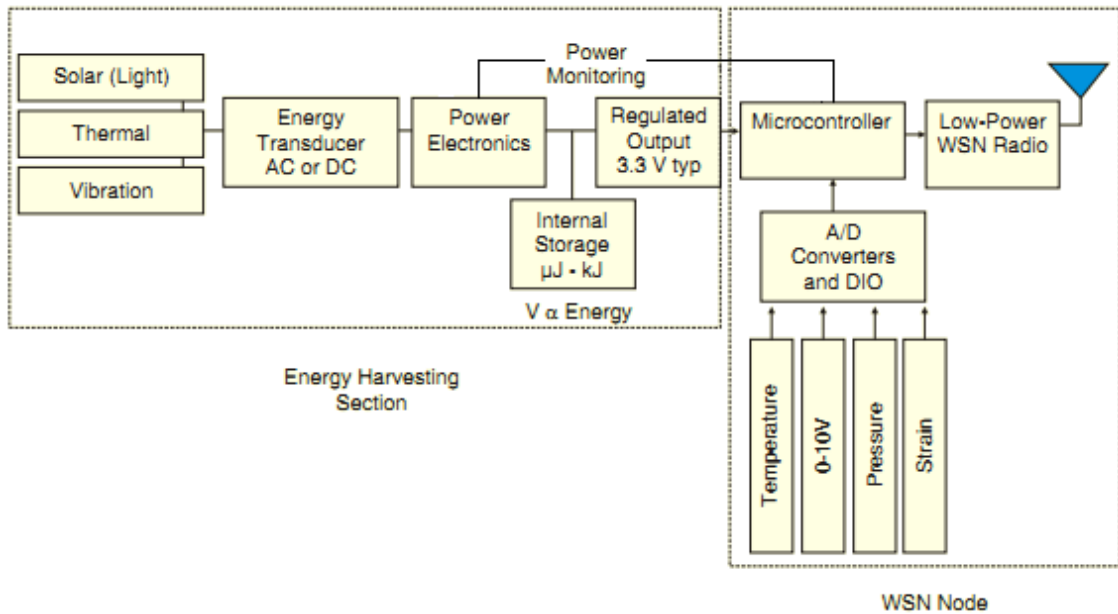


Figure 2.2: Proposed architecture for an Energy Harvesting Transducer [25]

energy harvesting systems is the AmbiMax Platform [19]. It offers a connection to a solar panel, a self-built wind generator and is capable of charging a lithium polymer battery. Every energy source is connected through a subsystem which consists merely of a boost regulator and a supercapacitor for buffering, see also Figure 2.3. To stay at the maximum power point of the solar cell but still keep the MCU in sleep mode, the MPP regulator is analog-controlled with comparators that are sensible to certain voltage thresholds.

Another project deals with a general design of a multi-source harvesting system for monitoring purposes [24]. The harvesting platform, called Managy, is a reconfigurable system that consists of various energy transducers, sensor interfaces and a digital Common Off-the-Shelf (COTS) microcontroller. To supply the load on two different voltage levels (1 V and ≈ 3 V) appropriate voltage conversion of the different energy sources is needed. In case of Managy, a photovoltaic cell, a thermoelectric generator, a vibrational harvester and a receiver antenna are used as energy sources. The battery is charged correctly according to its charge/discharge specifications by a monitored charger.

Information such as the State of Charge (SoC) can be useful in software implementations such as low power mode. It had been shown that this architecture can save up to 20%

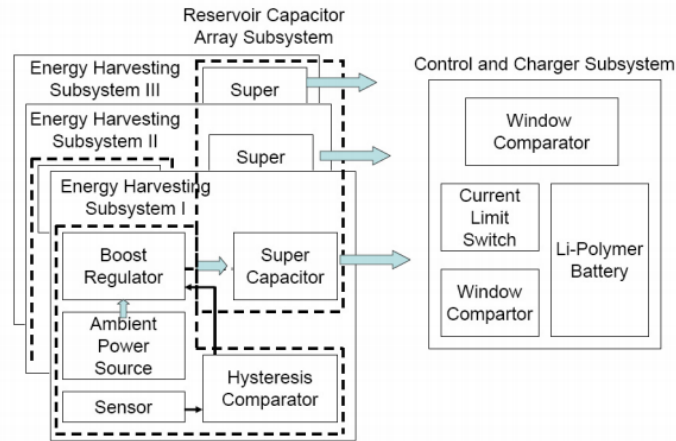


Figure 2.3: Energy harvesting system design of the AmbiMax project [19]

in normal conditions when using a double power path, separating low and high voltage modules.

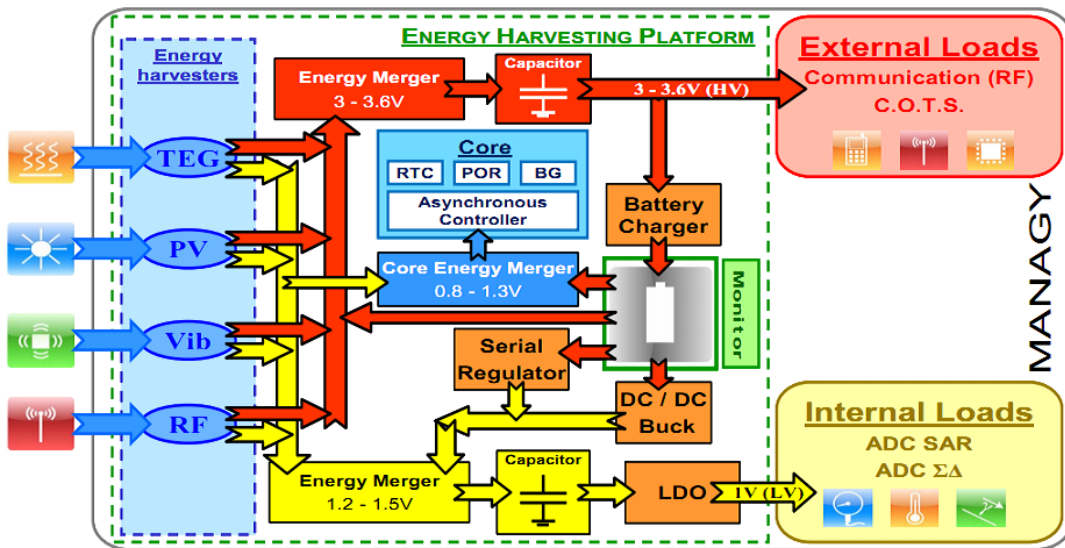


Figure 2.4: Proposed energy harvesting platform Managy [24]. The possibility to supply the load from five different energy sources makes it reliable in all situations.

2.1.1 Primary and Secondary Energy Sources

Since a genius scientist developed the idea of portable devices, batteries had been the alpha and omega for power supply and energy storage. Despite the fact that there are a

lot more energy buffers known nowadays, they are still the most favourable energy storage. If ultracapacitors keep the pace up of gaining higher power densities, they will substitute batteries one day.

Batteries

The biggest problem of batteries is the environmental harm of the disposal. This makes them not ideal for application in high integrated sensor dust networks with hundreds of nodes. Another disadvantage is the relatively complex recharge process that will not apply to capacitors and the invalidity of the Moore's law. Whereas the integration density is doubling every two years, the battery technology is stuck and only 3% of progress is made per year. Maybe the biggest advantage and the reason why batteries are still widely used, is the high storable energy.

A system's lifetime is limited to the battery's lifetime. [23] states that actual deployments of sensor nodes indicate a shorter lifetime than expected due to premature exhaustion of batteries through more or less four effects: Aging, memory effect (not for all types of batteries), pulsed discharge with following recovery effects and thermal effects. Furthermore, rate capacity effects are important to consider in which high discharge currents cause inactive sites on the cathode leading to a reduction in battery capacity.

Interestingly, [23] also stated that in absence of a voltage regulator the transmission power levels of wireless communication modules degrades.

Ultracapacitors

Today most supercapacitors come in the design of double layer capacitor in which carbon-based electrodes are separated through an organic electrolyte. This is the third class of capacitors, following capacitors with a dry (first) and a moist (second) separator. Achievable capacitances lie within a dozen Farads.

In [20] a solar harvester used a supercapacitor for energy storage after a few tests of lithium polymer and NiMH batteries had revealed their weakness of poor performance in lifetime and capacity at lower ($< -30^\circ$) and higher temperatures ($> 70^\circ$). The tests had only little influence on the parameters of the supercapacitor. The only problem was that this type of capacitor worked fine with 2.5 V, so if a higher voltage rating was desired, one would need more elements in series resulting in a lower capacity. The calculation of caps in series will result in similar calculation of resistances in parallel.

Another project [21] likewise used a supercapacitor as energy storage but had to use a pulse frequency modulation regulator to simultaneously keep the solar cell at the maximum power point and charge the capacitor. They expected the lifetime of the Everlast Node to be over 20 years because of the high recharge cycles and low degradation of the supercapacitor.

In [22] a few pros and cons of supercapacitors are listed. Among the most famous pro arguments are the very high cycle life, high specific power, simple charging procedure and the charging cycle can be done within seconds. On the drawbacks one can mention the low specific energy, high self discharge, low cell voltage and, in comparison to batteries, high cost per watt hour.

Batteries vs. Ultracapacitors

Summing up the advantages and disadvantages of batteries and supercapacitors, one can say that the supercapacitors are a leap ahead of the batteries. Along their easy charge / recharge cycles and little degradation, they possess the potential to displace batteries. The only real advantage of batteries is the high capacity. In conclusion, an overview of different types of batteries and ultracapacitors is given in Table 2.1.

Table 2.1: Overview of most common batteries and their attributes compared to a supercapacitor. Values taken from [17][22]

	Avail. Size	Rech. Cycles	Self Discharge	Ambient Temp.
Lead Acid	up to 200 Ah	1000	3-4 %/Month	-20°C to +60°C
Nickel-based	85 Ah	1000	10-15%/Month	0°C to +65°C
Lithium-based	over 3000 mAh	500 - 2000	5 %/Month	0°C to +65°C
Supercapacitor	1000 F $\hat{=}$ 695 mAh	100.000	50 %/Month	-45°C to +125°C

2.1.2 Harvesting

When it comes to wireless sensor nodes one will always find the keyword harvesting. Imagine a wireless sensor network that monitors a city's sewage system which is not very accessible. So if batteries and capacitors are used for power support, the maintenance costs would explode. They are crucial for long lifetime and maintenance-free solution approaches. By using a combination of harvesting and storing techniques, the lifetime of a sensor node can improve dramatically.

Energy harvesting techniques are often referred to as green energy because of their use of environmental energies:

- Solar Energy Harvesting
- Thermoelectric Electromechanical Harvesting (TEMG)
- Piezoelectric Harvesting
- Wind Power Harvesting
- Electromagnetic Harvesting (RF)
- ...

Taking the published energy values of [12][13][14][15] one can create a table to compare commonly used distinct energy harvesting techniques, see Table 2.2. Obviously solar energy and TEMG have the highest energy densities. A further positive aspect of these techniques is the relatively easy feasibility into the design.

Table 2.2: Overview of most common energy harvesting sources and their potential

Energy Source	Advantages	Disadvantages	Possible P_{out}
Solar	high power output, feasible to integrate	cost of production, disposal costs of used cells	10 mW/cm ²
Thermoelectric	there is always a temperature difference between air and soil	small power outputs, the better the higher the temperature difference	≈ 1 mW/K
Wind power	high power output	poor capability of being integrated in small systems, discontinuity of wind	kW to GW
Piezoelectric	no voltage source at node required	difficult to integrate in existing systems, small power outputs	4-800 μ W/Hz
Electromagnetic (RF)	no voltage source at node required	additional transmitting base station, power output can be changed within law limitation	≈ 13 μ W

Solar Power

Photovoltaic cells use solar power to produce energy in a complex recombination process. In the solar cell's years of childhood, one-layer silicon surfaces with power efficiencies of less than 10% had been used. Nowadays and with the advances in understanding of how they work, Bulk-Hetero-Junctions (BHJ) can be manufactured. For this purpose, three layers (red, green, blue) are put together, every single one with a different absorption maximum, resulting in a wider and evenly spread spectrum that allows for much higher conversion efficiencies. [12] states that photovoltaic cells are the most likely energy sources for integration in integrated circuits and power values of $10 \frac{mW}{cm^2}$ can be abducted. The official website of the Photovoltaic Centre of Austria [13] presents a huge dataset for all kinds of information about solar power. A very interesting insight is presented in Figures 2.5 to 2.8. For the GeoWSN, project it will be important to be able to draw the necessary energy to charge the battery as well as to supply the sensor node from the solar cell. Although the point of maximum output power is at about 30° south in Figure 2.7, it will be better to incline the cell to 45° to obtain higher power outputs during the winter season.

Thermoelectric Generators

The big advantage of Thermoelectric Generators (TEMG) is the fact that this power source is always available if there is a temperature differential. It is very common to dig one side (heat sink) into the ground and to leave the other side (cold side) surrounded by ambient air flow.

The thermoelectric module converts a temperature difference in a voltage via the Seebeck

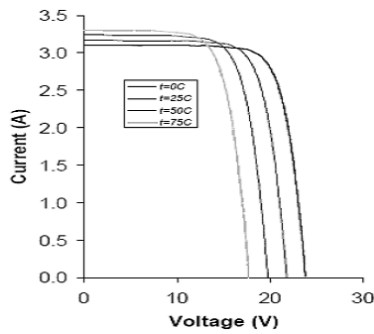


Figure 2.5: Temperature influence on position of maximum output power, BP-350U datasheet

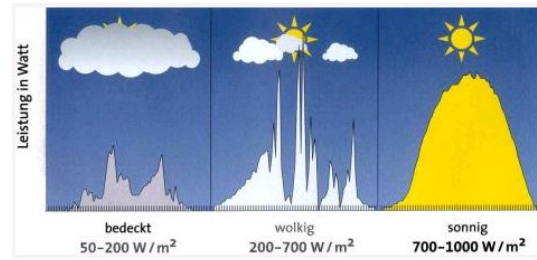


Figure 2.6: Incident solar power under different weather conditions, [13]

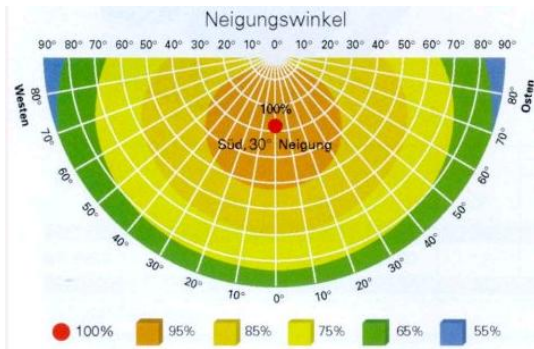


Figure 2.7: Average Power output of a solar cell that is inclined under an angle α in a certain geographic direction per year, [13]

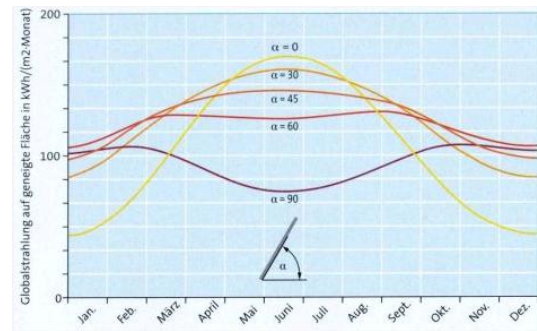


Figure 2.8: Power output of a solar cell inclined under an angle α [13]

effect. The module is sensitive to polarity, so if the sides are swapped, the output voltage changes its polarity.

Today, most available thermoelectric modules are made up of pairs of n-type and p-type semiconductors [6] that are connected in series. These semiconductors are highly optimized in respect to the Seebeck effect. Sizes can range between 10 mm and 50 mm for the sides and a few mm in height.

Increasing the output voltage, needs

- a higher temperature differential: 10 mV/K to 50 mV/K at the output
- more pairs of n- and p-type semiconductors
- lower source resistance: the standard would be 0.5 Ω to 5 Ω , putting more pairs in series will result in a higher source resistance and a higher voltage drop in use

To increase the output power we have to match the load. As we can see in Figure 2.11, the open circuit output voltage of a TEMG is very low. For this purpose, Linear Technologies (LT) developed the LTC3108, a DC/DC converter designed for ultra-low voltage input. This reveals the possibility for charging a supercapacitor or a small battery from

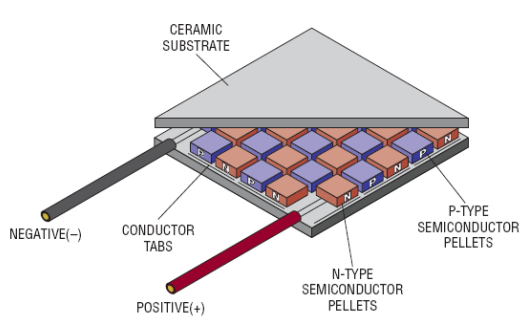


Figure 2.9: Composition of a semiconductor TEMG, [6]

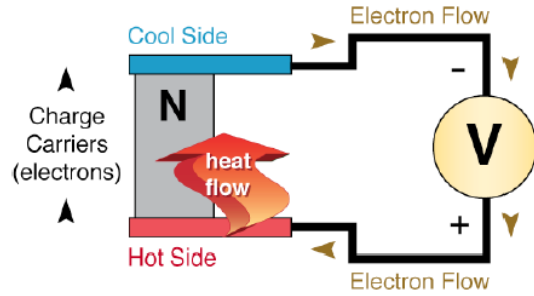


Figure 2.10: The operating principle of an n-type semiconductor in a thermoelectric module, [7]

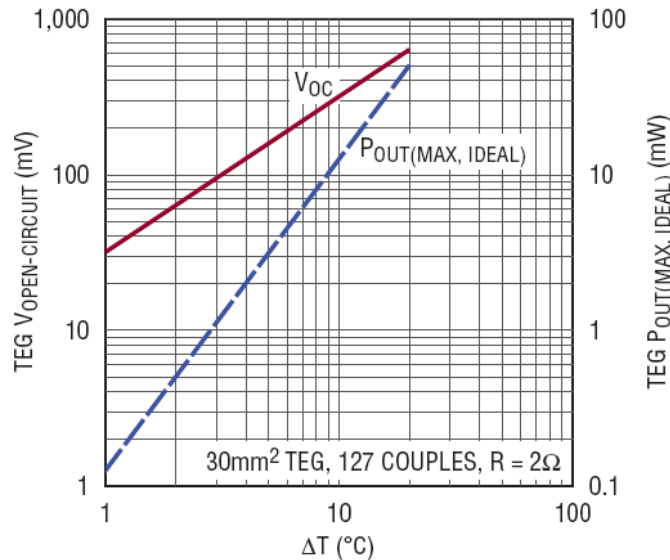


Figure 2.11: Expected output power and open circuit voltage of a thermoelectric module, [6]

temperature differentials as low as two degrees. There is already LTC3109 as LTC3108's successor on the market. With this IC, autopolarity energy harvesters can be built but this will cause a higher necessary temperature differential.

Electromagnetic Harvesting (RF)

In [10], another possibility of energy harvesting is presented. In this approach, electromagnetic waves from radio or television broadcasts are used to supply the sensor. This would be a huge advantage compared to solar cells due to the permanence radiation of the electromagnetic waves, independent of night-day cycles.

At the input of a rectangular antenna is a more or less simple bandpass filter that selects the channel in which maximum power is supplied to the node. Afterwards, a charge pump

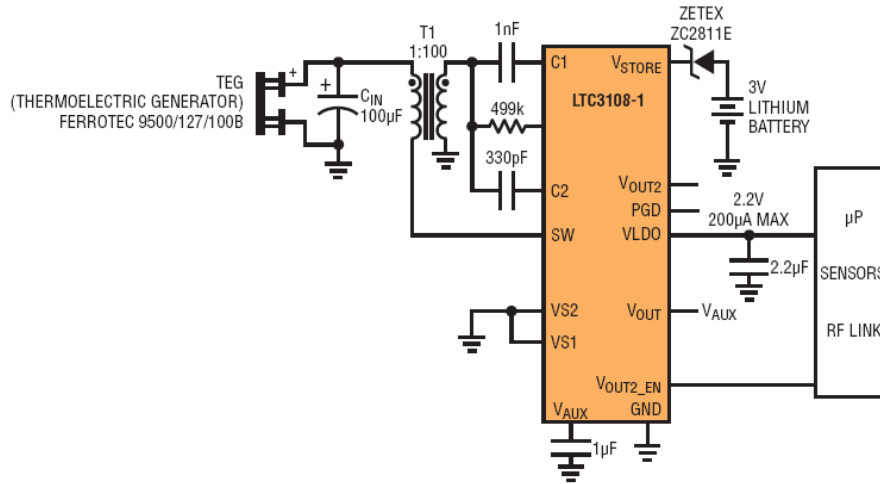


Figure 2.12: Electronic circuit for charging a 3V lithium battery from a TEMG input with the LTC3108 DC/DC converter, [6]

in Villard- or in Cockroft-Walton configuration will boost the input voltage adapted to the necessary voltage level. Results of $8 \mu\text{A}$ in the 1.542 MHz band and for the charge pump in Villard configuration are predicted. Although this result is quite promising, commercial use is prohibited in Austria due to law limitations.

Nevertheless, there is a permitted solution presented in [18]. A base station transmits in the ISM band within law regulations and is used by the sensor node to power its electronics. To calculate the received power at the node in a distance R one can use:

$$P_r = \frac{P_0 \cdot \lambda^2}{4 \cdot \pi \cdot R^2} \quad (2.1)$$

whereas P_r is the received power at the node, P_0 the transmitted power of the base station, λ is the wavelength and R the distance between the source and the sink. A distance of 5 meters in the ISM band would result in $50 \mu\text{W}$ at the receiver.

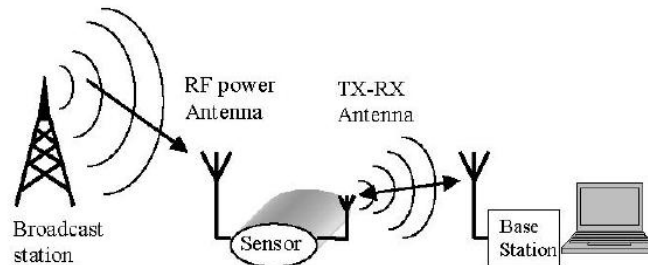


Figure 2.13: Possibility for using electromagnetic radiation from the environment [10]

2.2 Maximum Power Point Tracking

MPPT is the abbreviation for "Maximum Power Point Tracking" and means to track a certain point on the voltage current characteristic in which maximum power is delivered to the load. The problem is that this important state varies in temperature and has different irradiation levels [1]. This leads to the necessity to track it manually to provide maximum power to the load and to avoid load mismatch. MPPT is not only important for Wireless

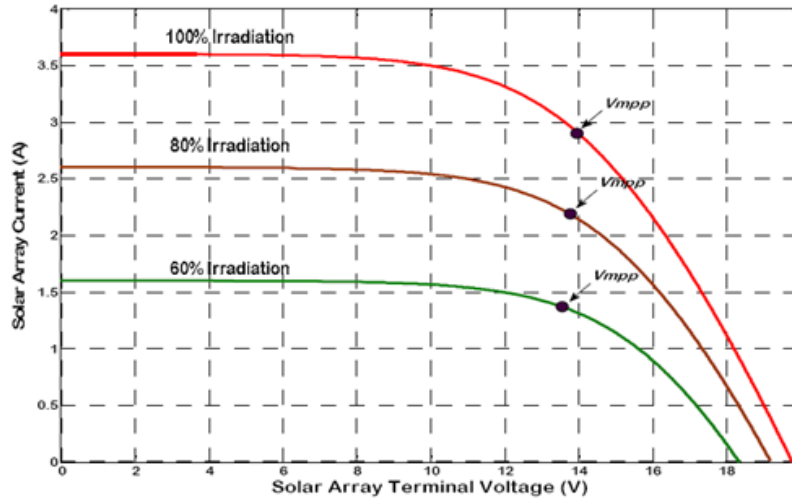


Figure 2.14: Maximum Power Point Tracking at different irradiation, [1]

Sensor Networks where power consumption is crucial to life time, it plays also a major role in industrial applications where huge photovoltaic cells are in use and just a little load mismatch can result in heavy power losses.

Calculating the efficiency with the actual electrical characteristics, gives an idea how close the system is to the MPP:

$$\eta_{MPPT} = \frac{\int_0^T P_{actual}(t)dt}{\int_0^T P_{max}(t)dt} \quad (2.2)$$

For this purpose a few methods had been developed:

- **Pilot Cell:** With changing temperature conditions or a cloud blocking sunlight, the MPP changes and normally the photovoltaic cell has to be disconnected to determine the new MPP. Use of huge solar panels leads to tremendous power losses. To avoid this problem, [2] used a little pilot cell in open circuit configuration.

The knack is the relation of the open circuit voltage V_{oc} to the voltage at the maximum power point V_{MPP} . Identically constructed photovoltaic cells have the same ratio independent of their size, so determining the MPP of the small solar cell will give the MPP of the big panel. Figure 2.15 shows a typical architecture of MPPT with a pilot cell.

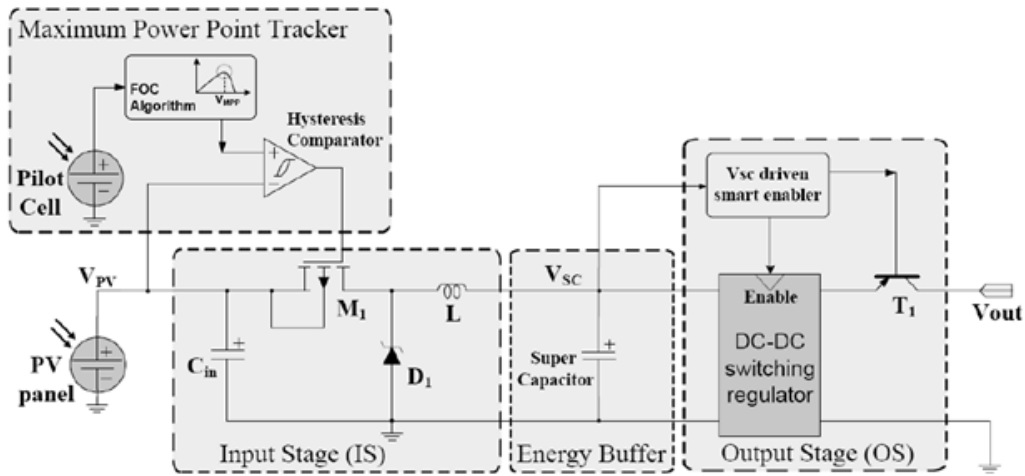


Figure 2.15: A representation of a Pilot Cell Maximum Power Point Tracking architecture, [2]

- Fractional Open Circuit Voltage or Short Circuit Current:** For this purpose the voltage or the current are regulated with a constant factor. This fractional ratio is defined by the open circuit voltage, or respectively, the short circuit current. Looking at Figure 2.14 one can see that the ratio of $\frac{V_{oc}}{V_{MPP}}$ stays nearly constant. Although the integration of these method is quite feasible, tests had shown a significantly worse performance compared to the Perturb-Observe as well as the Incremental Conductance algorithm, see Table 2.3.
- Linear Shunt Regulation:** In normal mode the shunt resistor is inactive and connected if excess power is available. Most of the implementations are designed with an hysteresis comparator and a MosFET. Through its simplicity, it is an often-used MPP technique, but one also has to consider the high amount of excess energy which is turned into heat.
- Adaptive System:** In this case the mathematical characteristic of the solar cell is modeled digitally. To determine the correct MPP the input and output voltage / current plus the light intensity is measured. Afterwards the DSP calculates the MPP through a predefined model and controls the gate of a MosFET. By varying the Duty Cycle, the system gets closer to the MPP, see also Figure 2.16

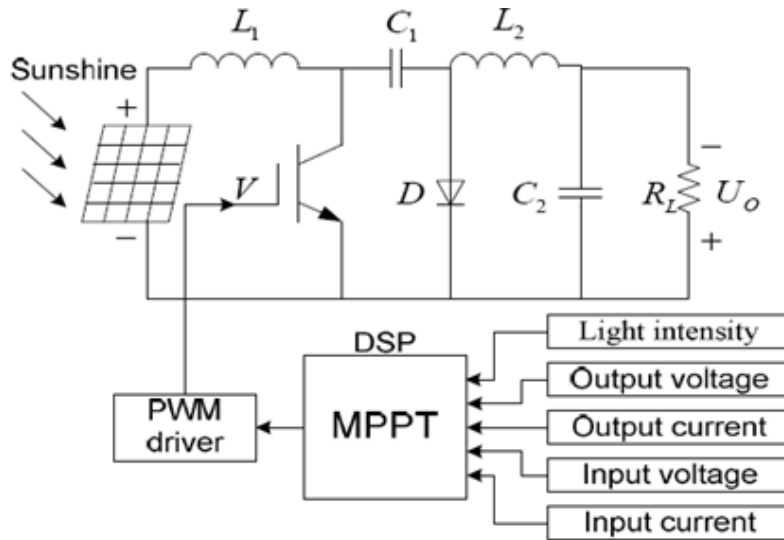


Figure 2.16: Representation of an adaptive system to track the MPP, [3]

- Perturb and Observe:** This is the most common technique to track the MPP [4]. The theoretical background is if after a perturbation at the input, the ratio $\frac{dP_{out}}{dV_{in}}$ is greater than 0, the system got closer to the MPP. So by perturbing the input and measuring the available power at the load, one can easily say what is necessary to get the system in the MPP. A Problem mentioned in [4] is the oscillating behaviour.
- Incremental Conductance:** To avoid the oscillating behaviour of the Perturb and Observe Algorithm, [5] describes a different approach. Being aware that at the MPP the derivative of $\frac{dI}{dV} = -\frac{I}{V}$ and $\frac{dP}{dV} = 0$, there is no need to perturb the input. So by measuring the differences of the current and last value, one can say whether the system is in MPP or not. See Figure 2.17 for the whole sequence flow. A problem is given by its complexity and the need for fast processors, but showing off a very good performance, see Table 2.3.

Table 2.3: Overview of measured and calculated efficiencies of most common MPPT techniques, [4]

	Perturb and Observe	Incremental Conductance	Fractional Open Circuit
Array	96.5%	98.2%	88.1%
Simulator	97.2%	98.5%	92.7%

2.3 Power Converter

The most important task of an energy harvesting system is the regulation of the incoming, or rather the harnessed energy. Depending on the application, one can first distinguish

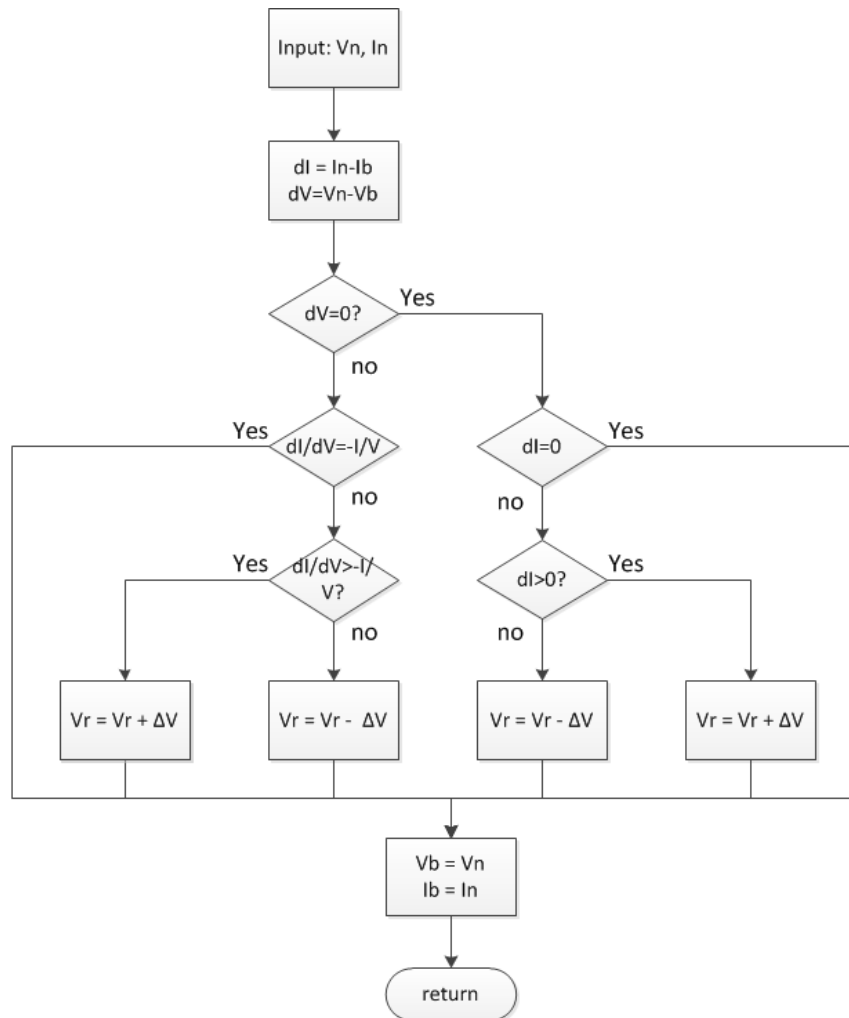


Figure 2.17: Sequence flow of the Incremental Conductance Algorithm, [5]

between a low drop-out voltage regulator (LDO) and a DC/DC Converter. LDO's have the advantages of a lower minimum operating voltage and a higher efficiency operation. Selecting the right converter topology for an application is often a difficult task. In [9], one finds advice and a few selection rules for this purpose. Especially the following design boundaries have to be considered:

- Charge Current
- Voltage Range
- Ambient Temperature
- Desired Switching Frequency (determines the size of an inductor)
- Available PCB Area

One may also decide if the converter will operate synchronously or non-synchronously. Both have their advantages and drawbacks, but most designs use non-synchronous topologies because of their feasibility to only implement one switch. Synchronous converters use two switches (MOSFET) and have to use break before make to avoid high short currents when both switches are conducting. Power losses in the freewheeling diode limits the charge current in the non-synchronous topology. The choice of NMOS or PMOS determines the application. An outstanding overview of all normalized DC/DC regulators is given in [8].

For this Master Thesis only the buck, boost and the SEPIC converters were of interest and suitable for the application area. The Split-Pi Converter would have been a very interesting option too, but was dismissed in the evaluation process and should just be mentioned here for the sake of completeness.

2.3.1 Buck Converter

This type of converter regulates the input voltage to a smaller output voltage that is directly proportional to the duty cycle D :

$$V_{out} = D \cdot V_{in} \quad (2.3)$$

Here one would need a high side driver when using a NMOS Transistor. A problem emerges when using PMOS: As long as there is logic low on the gate contact, the load is attached to the input voltage. Most recent projects used this type to regulate the input voltage of a solar cell to the charge voltage of a battery pack [4]. A schematic representation of this converter type can be found in Figure 2.18.

2.3.2 Boost Converter

In contrast to a buck converter, a booster regulates the output voltage to a higher value than the input voltage and is again controlled by the duty cycle D , see Figure 2.19:

$$V_{out} = \frac{1}{1 - D} \cdot V_{in} \quad (2.4)$$

Care has to be taken that the output cannot be disconnected from the input, therefore resulting in currents, flowing from the input to the output in undesired cases if using this design.

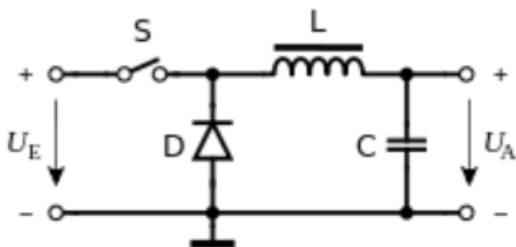


Figure 2.18: Basic Buck Converter, [8]

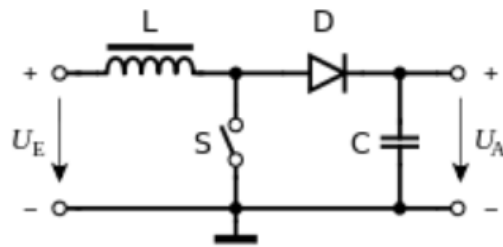


Figure 2.19: Basic Boost Converter, [8]

2.3.3 SEPIC Converter

In Figure 2.20 overcomes the SEPIC Converter the major drawback of a buck/boost converter: The output voltage is not inverted. Furthermore, it removes unwanted noise from the input through the capacitor between the coupled coils and also isolates the output from the input. Controlling the duty cycle D of the switching transistor defines the output voltage:

$$V_{out} = \frac{D}{1-D} \cdot V_{in} \tag{2.5}$$

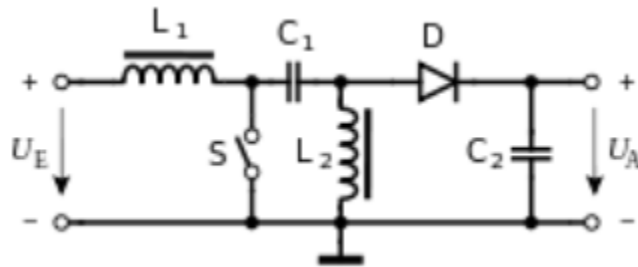


Figure 2.20: Basic SEPIC Converter, [8]

2.3.4 Split-Pi Converter

A very interesting approach is the synchronous Split-Pi Converter. With this Power Converter it is possible to have an energy flow in both directions, which is not possible with all the other converters and is used, for example, in an electric kart drive [11]. The control of the MosFETs to switch properly must fall to a DSP because other MCUs would not be fast enough to handle the synchronicity. Asynchronism bears the danger of high short currents if there is an overlap of the conducting region between the switching MosFETs. A PSPice model of a Split-Pi converter can be found in Figure 2.21.

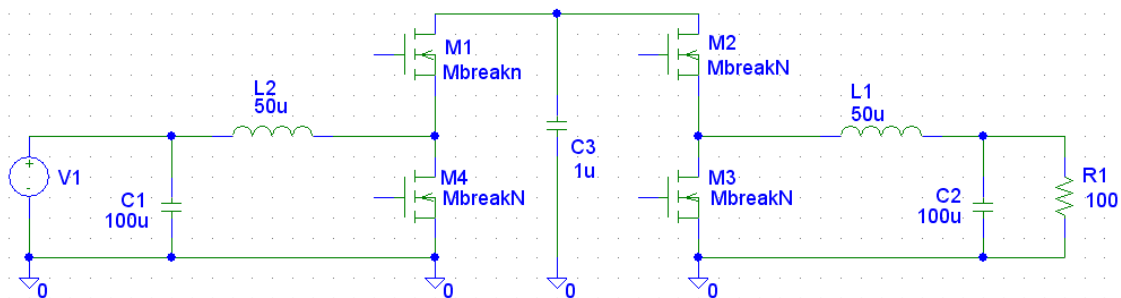


Figure 2.21: Simulation of a Split-Pi converter in PSPice 8

2.3.5 Electronic Control Unit

To keep the output voltage regulated, there is always an electronic control circuit implemented. The control loop has the duty to adjust in case of voltage fluctuation on the input or changes in load current. This is often referred to line and load regulation. Most common techniques are current- and voltage-controlled:

Using current mode regulation, one controls the current through the inductor directly and in first approximation the charge current into the output capacitor. This is equivalent to the output voltage. However, for voltage mode control one controls the duty cycle of the switch, hence, the voltage over the inductor. Subsequently, the current through the inductor changes and thus the output voltage. This means also that the control path of the regulator is in voltage mode control of second order, whereas for current mode the control is only of first order. This is likewise the reason why the last one is preferred.

2.4 Summary

In this chapter much work related to mobile energy management is discussed. First of all, energy management has to be divided in a part of harvesting and in the conservative part of storage. This will not only prolong the lifetime of the sensor node, it will also reduce or even avoid the disposal costs for empty batteries. The energy storage is limited to battery and supercapacitors, whereas lead acid batteries seem to be the best choice regarding their energy storage capability, recharge cycle and low temperature usability. Although ultracapacitors would have a lot advantages, the problem of low operating voltage still puts batteries into pole-position.

To operate the photovoltaic cell at the maximum power point, the switching regulator will most likely be of type Buck or SEPIC converter and current mode-controlled. The tracking of the MPP can be done with several algorithms and techniques. The most promising approaches are the simple fractional open circuit and the more complex Perturb and Observe.

For now there is no documented literature on reverse current mode of photovoltaic cells in WSN applications, so it has to be tested before implementation.

Chapter 3

Solution Approaches

This chapter is about the design and solution approaches for implementing a high efficiency Energy Harvesting System (EHS) for landslide monitoring. In an earlier Master Project a wireless sensor node hardware had been developed and will be put together with the EHS into a waterproof case.

In the previous section, various system designs were discussed, whereas this project needs a different approach due to reverse current operation of the photovoltaic cell. For proper and probably maintenance-free operation of the system, a few factors have to be kept in mind. Furthermore, design requirements had been specified or were requested for information processing:

- Reverse current mode to keep the solar cell free of snow
- Keeping track of the maximum power point
- Possibility to add more energy sources to the grid
- Measurement of the actual charge state of the battery and transmission to the sensor node over a serial interface
- Power supply sensor node
- Efficient management of an energy storage device

These design factors will be discussed in the following subsections.

3.1 Energy Sources

Due to the high power consumption of the Sensor Node [16], a battery as energy storage will be insufficient. Another benefit of going towards energy harvesting would be the longer lifetime and the reduced costs of maintenance. The drawbacks of powering the sensor node only with energy harvesting are pretty obvious, because of the impermanence of natural energy sources. Solar cell-powered sensor nodes have a serious problem during nights and long winters where direct sunlight cannot be observed.

For this project, a combination of energy harvesting and energy storage in form of an accumulator will be considered.

3.1.1 Energy Harvesting

Solar cells deliver the highest output power of all alternative energies. Further advantages of this energy source are the good periodicity of night - day changes and the possible high output currents of a few Amperes which make them ideal for battery charging.

Another possible candidate for delivering power to the load is thermoelectric harvesting. In contrast to a solar cell, its output power is relatively small but has the same periodicity. Especially in autumn or spring, there is the possibility of very high temperature gradients and output power could increase significantly. A further investigation and a measurement setup will give conclusions on whether it makes sense to use a thermoelectric harvester or not.

Other sources cannot be used due to the lack of vibrations (piezoelectric) or the non-periodicity of wind power. The calculation of size for the photovoltaic cell is shown in 4.1.1.

3.1.2 Energy Storage

To power the load and store the harvested energy, an energy storage device like a rechargeable battery or a supercapacitor has to be used. As mentioned in the previous chapter 2.1.1, they have both advantages and disadvantages. Batteries persuade with the high specific energy and the low discharge current. Capacitors score with fast and nearly unlimited charge cycles and the possible feasible integration.

[16] states that the maximum load current to supply the sensor node with activated GPS, GPRS and transmitting to a base station, a total of 408 mA peak current with a 3.4 V voltage supply is needed. Considering one of the biggest supercapacitors available with a capacitance of 1000 F and a 2.5 V voltage rating would only deliver

$$Q = C \cdot U = 1000 \text{ F} \cdot 3.4 \text{ V} = 3400 \text{ As} = 3.4 \cdot 10^6 \text{ mA} \cdot \text{s} \quad (3.1)$$

This would result in a theoretical supply time of

$$t = \frac{W}{P} = \frac{\frac{1}{2} \cdot Q \cdot U}{I_{load} \cdot U_{load}} = \frac{0.5 \cdot 3.4 \cdot 10^6 \cdot 2.5}{408 \cdot 3.4} = 3063.7 \text{ s} \approx 0.85 \text{ h} \quad (3.2)$$

Conducting the same thought experiment for a relatively small 12V, 2Ah lead acid battery, one can obtain a supply time of

$$t = \frac{\frac{1}{2} \cdot Q \cdot U}{I_{load} \cdot U_{load}} = \frac{0.5 \cdot 7.2 \cdot 10^6 \cdot 12}{408 \cdot 3.4} \approx 8.7 \text{ h} \quad (3.3)$$

outnumbering the capacitor by a factor of 10 and still possessing the possibility of choosing a bigger battery. So for this project, a battery-powered supply is chosen.

Comparing different battery technologies (see Table 2.1), one can see that Lead Acid (LA) batteries are the best choice for this project, where the sensor will be in a harsh environment most of the time. Calcium-based batteries would have been a good choice too, but have the problem with a complex charging procedure. If the calcium battery is not charged with 15.8 V a phenomenon called acid layering occurs, resulting in a low capacity and lifetime [26]. However, these are much cheaper than lead acid batteries. The size of the necessary battery is calculated in 4.1.4.

3.2 Hardware Design

For power management in hardware design two main strategies have been considered:

- Split-Pi converter
- MPP-controlled Buck or SEPIC converter

The Split-Pi converter is a promising approach where it is possible to provide power in both directions. That would be very useful in our case where also an inverse current mode for the solar cell is needed. For this purpose, a buck and a boost converter in synchronous mode are put together. So it is possible to buck and/or boost a voltage in either direction just by switching the MosFETs appropriately. However, there is also a problem with this design. If the MosFETs are not switched correctly in time or the μC is stuck somewhere in the software, then high short currents can occur leading to the destruction of the EHS. Furthermore, an American patent protects the structure and the optimal switching behaviour of the MosFETs.

The more promising approach is to use an MPP DC/DC converter in one direction and another one for the reverse current mode. In the end, the system architecture should be comprised of five main parts: Energy harvesting, maximum power point controller, microcontroller, battery management and, finally, the power regulator to the load.

A few different approaches to energy harvesting have been studied and the solar cell seems to be the best choice. Another source with a lower output can be implemented right in front of the power regulator. The results of a study of Thermoelectric Harvesting will bring the decision for its implementation.

The Maximum Power Point Controller is a power regulator most likely of SEPIC type, so low power inputs can also be used to load the battery or supply the load. Characterization of the solar cell will give an idea if it is also possible to use a buck converter in case the input power is too low.

The core of the energy harvesting system is the microcontroller unit. Through input and output power measurements, it will track and keep the solar cell at its maximum power point. Furthermore, a serial connection with I2C or SPI is implemented for communication with the sensor node.

The output power regulator delivers the right voltage level and the necessary current to the load. Connect a low power output source here to supply the load.

3.2.1 Power Supply

The MSP430Fx series is working with supply voltages of 1.8-3.6 V. In [16], an operating voltage of 3.4 V had been chosen so a buck power converter between the solar cell and the microcontroller is needed. This demands a DC/DC converter with a huge input voltage range. It has to be investigated in a study if it is more efficient to regulate the voltage from solar input to 5 V and, subsequently, to 3.4 V or regulating it hard from the solar cell to 3.4 V. The idea is to create a dual power supply similar to the Managy platform [24].

3.2.2 Microcontroller

The heart of the energy harvesting system should be an economical microcontroller that supports enough computational power to calculate the necessary data for maximum power

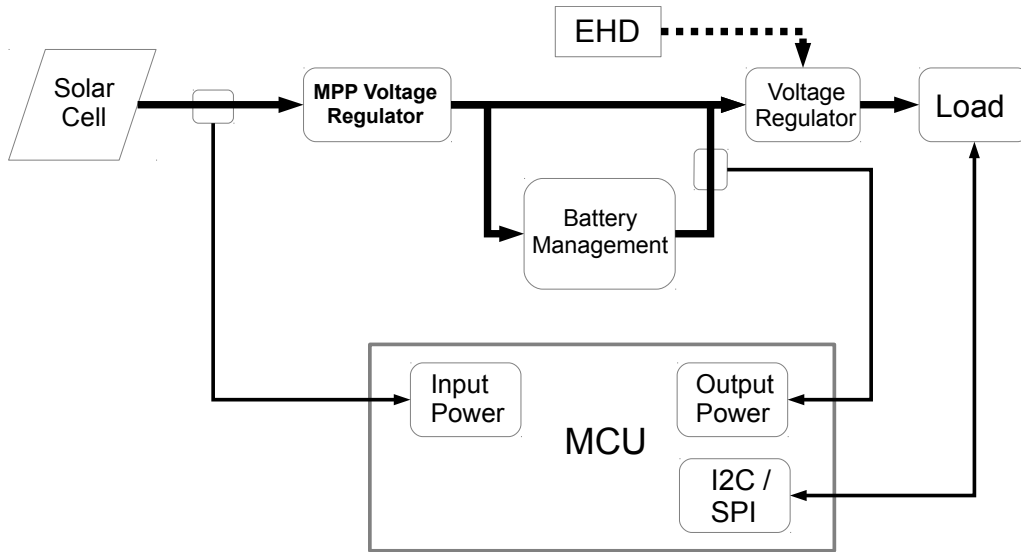


Figure 3.1: The basic concept of an energy harvesting system architecture, whereas the thicker lines show the energy flow and the thinner ones the information flow.

point tracking. Furthermore, there should also be an I2C interface for communication with the sensor node and enough I/O pins to control all modules on the board. To measure input and output power, there are also at least four ADCs needed. Controlling all of the DC/DC Converters will need a timer so one can create different PWMs to switch the gates of the MosFETs.

Due to the use of an MSP430F5438A on the sensor node, an MSP430F2274 from Texas Instruments will be used for this design. This microcontroller likewise supports programming over JTAG and is feasible to integrate. Comprising of twelve ADCs is a plus too. Power consumption of this IC is in active mode 14 mW while running on 16 MHz, in standby mode 2.4 μ W and is hence much better than, for example, an ATxmega256A3 with 20.7 mW in active mode and 9 μ W in standby mode.

3.2.3 Reverse Current Mode

Operating a solar cell in its reverse mode is not a novelty. SOLUTRONIC AG developed a de-icing box to de-ice large solar cells and, therefore, maximize power output during winter. This approach is covered by an international patent. A novelty is the use of the reverse mode in wireless sensor networks. Normally, a sensor node operates in lower power mode, but nowadays with increasing functionality and complexity, the available power rises to a level where it is even possible to de-ice the solar cell.

For this purpose, a test of the reverse current mode under different azimuth angles has been carried out. A power supply unit served as a source and the solar cell as a sink. The cell had been mounted on the north balcony of the Institute for Technical Informatics in Graz. In the range of the MPP of the solar cell, one could observe that the first snow layer on the solar cell became fluid and, therefore, nearly made the whole snow layer slip off the

cell. The influence of the angle was as one would expect: a larger angle causes the snow to slip off faster, but the energy yield of the solar cell highly decreases, see also Figure 2.7. Another interesting fact we discovered is the orientation of the solar cell. Normal-size solar cells are often built with a frame, so there is a problem when the snow layer begins to slide, see Figure 3.3. It would be better to rotate the solar cell by 90° so the influence of the frame is less.



Figure 3.2: Solar cell covered in snow before reverse current mode



Figure 3.3: Not the entire snow layer slid off, however, due to the frame

To replace the power supply unit, a battery as a source had been determined. The only question remained was how to create the desired voltage and current. The best way would be an LED-driver. The major drawback in this approach, however, is the commonly used sense resistor that would create a permanent power loss even if the reverse mode is not used. So a power regulator like a boost or SEPIC converter was chosen. The biggest disadvantage of the boost converter is that it is topology-based. The input can never be really disconnected from the load through the boost converter. During the night, where the potential of the solar cell is lower than that of the battery, a current will flow from the battery to the solar cell, draining the energy storage. A SEPIC converter can avoid this problem by disconnecting the output from the input.

3.2.4 Maximum Power Point Tracking

To ensure a proper load match between the solar cell and the sensor node and charge a battery correctly, a DC/DC Converter with a variable Duty Cycle has to be used. This converter is controlled by the charging IC which keeps track of the load on the source. A variable resistor is needed and has to be corrected according to the Maximum Power Point Tracking Algorithm, see chapter 2.2.

Another important key factor for the selection of the converter type is how much power will be available at the solar cell. According to the datasheet of the selected solar cell where the diagrammes had been quite confusing, a possible output power of 1.9 W at 10 V and $200 \frac{W}{m^2}$ irradiance level was specified.

Thinking in terms of charging a lead acid battery of the size of a car battery, this would not be very much. The used charging IC should not terminate until the charging current drops below a certain limit, so by using a buck converter there will be more problems.

It would arise that the battery cannot be charged if the input voltage at the solar cell is below the battery voltage because then the battery will supply the sensor node. Moreover input voltages below 10 V cannot be used to charge the battery. In this case a lot of power would be wasted.

Boost converters cannot be used here and buck-boost converters deliver an inverted output, so the only promising approach remains a SEPIC converter. The drawback lies within the difficulty to change the non-linear duty cycle and the higher component count. Feasible integration of a NMOS as low-side switch without the urge to use a high-side driver would be of benefit.

3.2.5 Battery Charging

To charge an LA battery correctly, a closed loop technique to terminate charging due to certain events is needed. The charging algorithm for lead acid batteries is very similar to that of lithium-ion batteries and consists of three charging stages [17]:

In the first stage, the constant current stage, the battery is charged with constant current until it reaches the absorption voltage that is one of the few important characteristics of a battery. Reaching this voltage leads to the second stage, the constant voltage charging. As the name implies in this stage, the voltage is kept constant and so the current decreases until a lower limit, the finishing charge rate. The last stage is the float charge stage, where the voltage of the battery is kept on another characteristic the float voltage. Now the battery is kept charged and losses due to self-discharge are balanced. See also Figure 3.4 for the different stages.

It is also said in [17] that the battery is fully charged when the finishing charge rate drops below of 3% of the rated current. This will not always be very practical, and so a lot of charging solutions offer a lower charge rate limit. In respect to the GeoWSN project, a problem can arise with the temperature because the float voltage and the absorption voltage are temperature sensitive and move towards lower (warmer temperatures) or higher (colder temperatures) values. This should be considered when regulating the voltages with a power converter.

In conclusion one can sum up some guidelines for the charging process:

- Absorption and float voltages are dependent on battery type and manufacturer
- Avoiding deep discharge
- Reducing or increasing the charge voltage characteristics depending on temperature

3.2.6 Connector

As the energy harvesting system is the main component of the whole system, there are a lot of connectors to consider. Connections to the energy harvesting and energy storage devices should be made with screw terminals that provide a solid and reliable connection. To communicate with the sensor node, an eight-pin connector will be installed on the PCB. This allows not only connections of power supply and ground, it also offers the possibility for adding I2C or SPI Bus and a few I/O Pins to configure.

Programming the μ C should be done via a JTAG interface and the Texas Instrument's

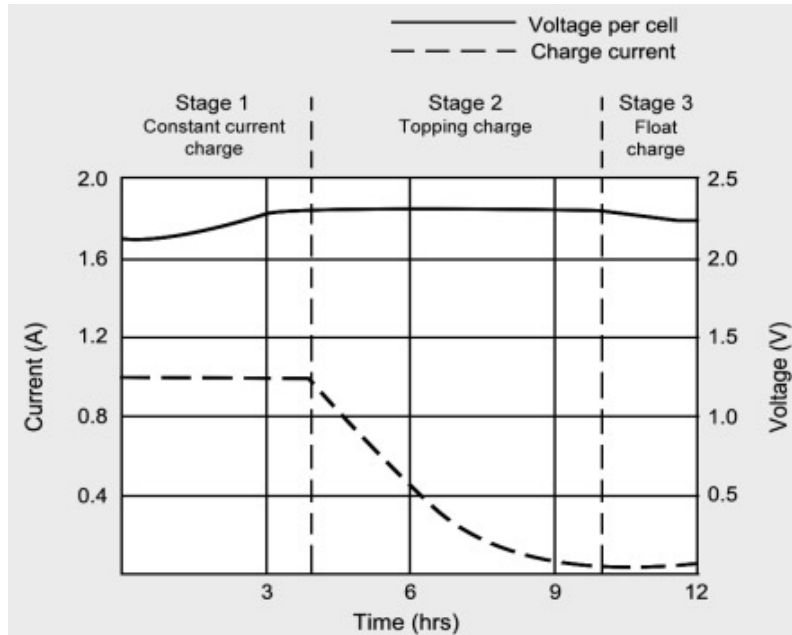


Figure 3.4: Voltage and current characteristics for charging a lead-acid battery [17]

Code Composer Studio. The configuration of the JTAG interface will be load-powered. To obtain qualitative results in the afterwards-following experimental results, a few 2 Pin Connectors are integrated, so that current measurements can be done for every module.

3.3 Software Design

This section describes the Software Design of the Energy Harvesting System. Programming is done in an environment called Code Composer Studio which is available and free for code up to 10kB. With version 4, the Code Composer Studio had been based on Eclipse, which is an open-source software framework. This integrated development environment is of perfect use for developing embedded systems. This studio has been developed by Texas Instruments and is, therefore, especially useful in combination with TIs DSPs, microcontrollers or other application processes. Just to mention a few features, it comes with a source code editor, project build environment and compilers for all TI devices that are currently available.

In contrast, the hardware design had been created in Eagle and is currently distributed by CadSoft, which is a subsidiary of the famous electronic distributor Farnell. Eagle is very efficient when it comes to PCB design and combines the schematic and the layout editor in one. It is also possible to use the autoroute function, so inexperienced users can also make their PCB dreams come true.

3.3.1 Maximum PowerPoint Tracking

In [4][28] and in chapter 2.2, an overview of MPPT algorithms is given. In this Thesis Fractional open circuit voltage and the Perturb-Observe algorithm are carefully studied. The fastest and most efficient algorithm will be used afterwards.

3.3.2 Activation Interval

When it comes to Wireless Sensor Nodes, the activation interval is of common concern due to its impact on overall lifetime. Normally a Sensor Node operates on a fraction of one percent Duty Cycle. In this project and the necessary always on, an activation interval cannot be defined.

3.4 Mounting

In a wide application area, electronic devices have to sustain functionality in industrial or harsh environments for many years. This often requires protection against dust, water and water vapour or oil. Several protection categories are defined in the EU norm DIN-EN 60529. In such a category, devices are evaluated for their acceptability to harsh environments and labelled with IP-xx. Whereas the first x describes the protection against foreign bodies or dust and the second x the protection against water and humidity. The abbreviation IP stands for International Protection.

Reviewing the application area of the GeoWSN project, which will be a more or less alpine environment, leads to a very high IP number. Total protection against contact and dust as well as protection against permanent ingress of moisture is an absolute must-have to fight against heavy rain or snow. This requires at least IP67, better would be IP68 but it is ultimately a question of price.

Furthermore, it is necessary to lead cables through to exterior-mounted antennas or sensors that will eventually harm the IP protection. Cable screw connectors will have to be used with the same IP classification.

3.5 Summary

In this chapter an overview of the design for the hardware and the software is given. First the energy source has been chosen where solar cells are the main source due to their high power output. The possibility of integrating a further harvesting device (EHD) like a thermoelectric generator is an option.

Due to the high power consumption of the node and the impermanence of the solar output, a battery was defined as energy storage. Best applicable is a rechargeable lead-acid battery because of the possible charging-discharging procedure at low temperatures. Calcium-based batteries had been considered but discarded by reason of the complex charging algorithm.

Third, the design of the energy harvesting system was discussed. To maintain the solar cell in its MPP, a switching regulator was chosen whereas its switching frequency is controlled. This change in switching frequency is done by measuring the input and output power that serve as input parameters to the maximum power point tracking algorithm. A further

investigation and comparison of different MPPT algorithms will give a better idea of which algorithm is best-suited for this application.

The chosen microcontroller is of the MSP430 series of Texas Instruments due to its low power modes and the feasible integration with the already existing MSP430F5438A on the sensor node. The communication between these two processors will be most likely I2C.

The design of the hardware is carried out in a software called Eagle. Within this software, the schematics and the layout can be created that will later on be used by PCB-Pool to print the circuit boards. The software design is completed in Code Composer Studio, a development kit from Texas Instruments. The programming language will be C and hardware units are described in classes.

Finally, a case, or respectively, mounting was chosen regarding the application area in alpine environment. The EU-Norm DIN-EN 60529 defines at least IP67 to be best suited. External antennas and sensors are connected to the case through cable screw connectors with same IP classification.

Chapter 4

Implementation

This chapter deals with the final implementation of the Energy Harvesting System in the GeoWSN project. It is divided into three main sections, whereas the first section is about the selection and calculation of the necessary components. In the second section, an overview of the implemented software, which is written in C, is given. The sequence control of the Microcontroller Unit is presented. Finally, in the mounting section the sensor node, the energy harvesting system and all of the other components (GPS, GPRS, ...) are placed in a case and prepared for monitoring a landslide-prone location.

The PCB layout is crafted by PCB Pool and the mounting of the Surface Mounted Devices (SMD) parts is done by hand. An SMD reflow kit [29] is used to solder the SMD parts on the PCB board. Using this technique, soldering effects like tombstoning occur, whereas an SMD part is only soldered on one side and swelled on the other side through the temperature. This effect could not be observed.

The width of the PCB track and the current capability have been calculated according to the PCB Pool specification [30].

4.1 Hardware

In the final design of the EHS, a MSP430F2274 microcontroller controls the behaviour of the single modules. Due to the availability of I2C on this processor, this will be used for communication with the sensor node. Programming is possible in the Code Composer Studio with the JTAG interface. With this component, it is possible to switch off every module and, thereby, control the SEPIC converters and the charging procedure.

A solar cell has been chosen as the energy source which will be operated at the maximum power point by a regulated SEPIC power converter. The whole maximum power point control is achieved by the LTC4000-1 and a variable digital potentiometer (MCP4152). The necessary resistor size is calculated and written over SPI to the potentiometer by the microcontroller. The calculation of this resistor depends on the used MPPT algorithm and the input-output power measurements which will be made with current shunt monitors from Texas Instruments. A following 3.4V DC/DC converter supplies the sensor node with the right voltage level.

The energy storage is an 20 Ah lead acid battery controlled by the LTC4000-1 charging IC from Linear Technologies. In combination with the SEPIC power regulator and the

MSP430 microcontroller, one can define special charging procedures making it possible to use different algorithms and batteries.

Another very important part of the EHS is the reverse current mode. As mentioned in the last chapter, an LED driver did not fulfil our requirements in terms of power efficiency, so another SEPIC converter is used. This converter is supplied by the lead acid battery and switched on/off by a pulse width modulated signal provided by the microcontroller.

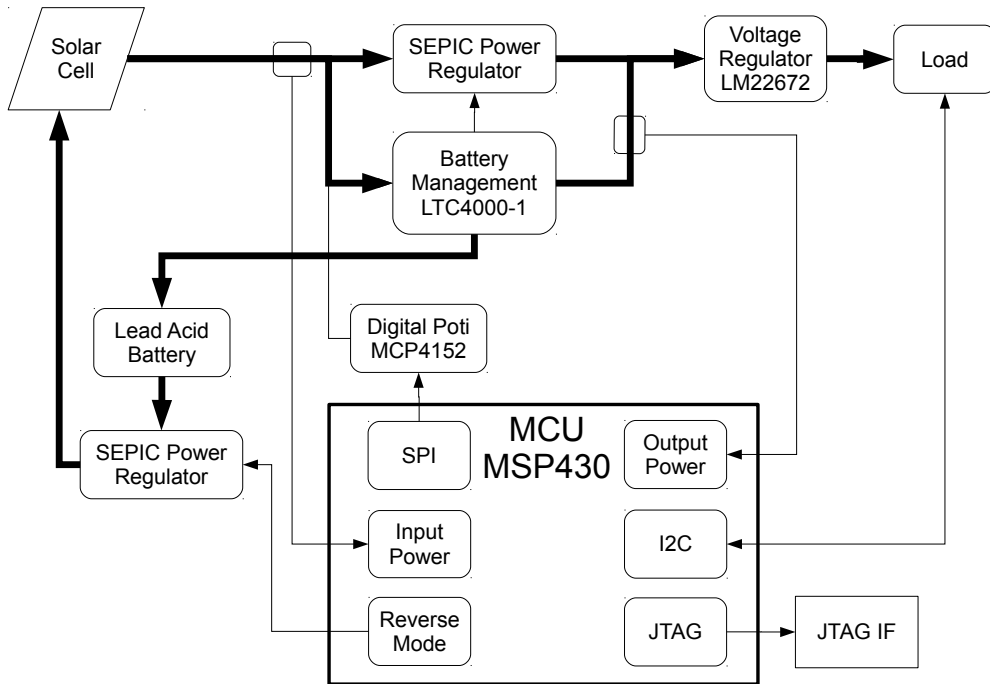


Figure 4.1: Implemented Design of the Energy Harvesting System. Bolt arrows show the energy flow, whereas the thin arrows show the information flow.

4.1.1 Energy Sources

A photovoltaic cell and a thermoelectric generator were planned as energy sources. [16] states the power consumption of the sensor node. The maximum power needed is 1386 mW and the minimum is 706.6 mW (without GPRS). So the energy sources have to deliver at least 707 mW. In [31], tests to implement a thermoelectric generator (TEMG) in two different designs had been carried out. The first architecture of the generator is illustrated in Figure 4.2. Due to deployment in mountain areas, the soil will be the heat source and the air will work as a heat sink. The heat pipe is made from copper and is insulated to achieve a higher temperature differential between the two ends of the TEMG. The heat pipe is filled with acetone and rammed 1 meter into the soil. The second composition is a heat box filled with water and anti-freeze fluid, see Figure 4.3. The heat pipe is again put into this mixture. This architecture has the advantage of a shorter heat pipe.

Furthermore, one does not need to make a hole in the ground, which is especially useful for applications in landslide-endangered hillsides. Some of the results and the measurement set-up are presented in the Figures 4.2 to 4.5.

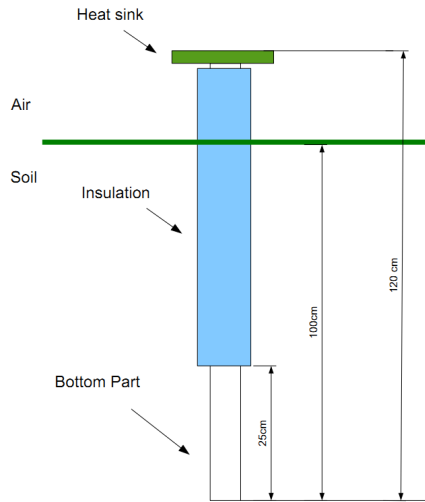


Figure 4.2: Basic architecture of the thermoelectric generator [31]

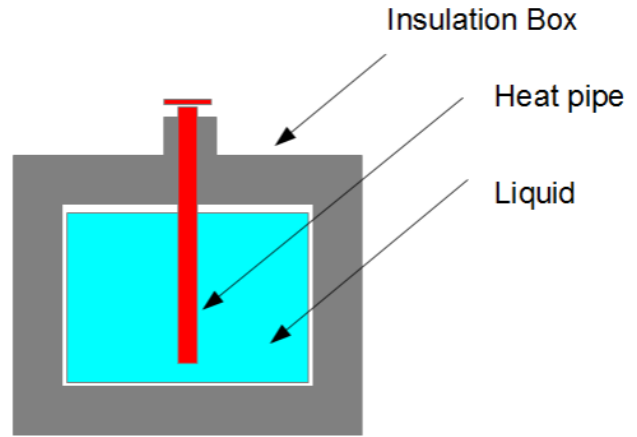


Figure 4.3: Basic architecture of a TEMG with a heat box [31]

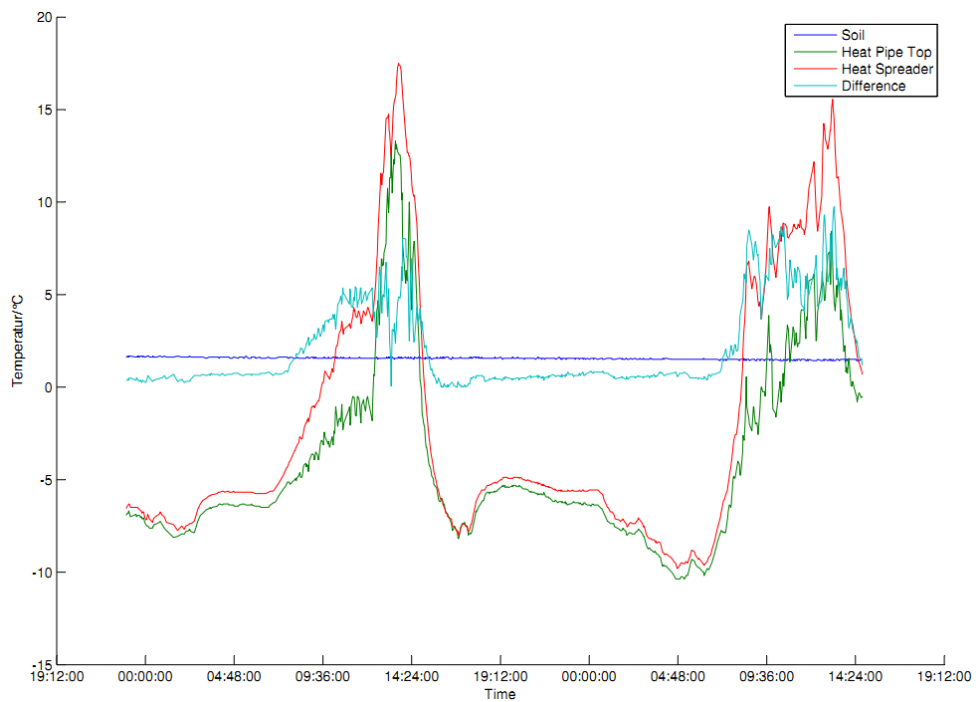


Figure 4.4: Measuring the temperature difference between soil and top of a heat pipe, [31]

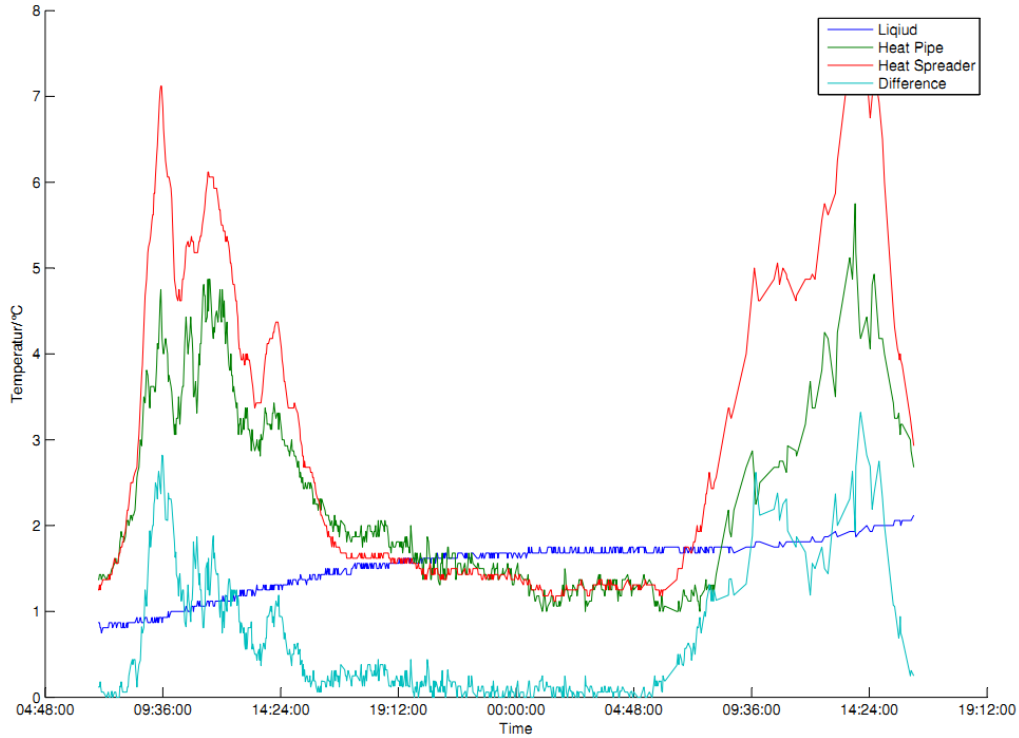


Figure 4.5: Heat box. Measuring the temperature difference between the liquid and top of the heat pipe, [31]

From Figures 4.4 and 4.5 one can see that the temperature difference between the soil and the top of the heat pipe was too little to be able to use it efficiently. Although the LTC3108 could start from a difference as small as 1 °C, the power output would be tiny in relation to the requirements. Nevertheless, the more promising approach is the primary design where the heat pipe is rammed into the soil. Therefore only a lead acid battery and a solar panel have been considered as energy sources.

Calculating the necessary size of the battery, one would consider [27]:

$$C = \frac{A \cdot W_{av}}{U_N \cdot \eta} \quad (4.1)$$

whereas A holds the number of days where the sensor node is supplied solely from the battery without recharging, W_{av} is the average power consumption per day and U_N the supply voltage. Considering a permanent three days ($A=3$) supply solely from the battery and a continuous power consumption of 706.6 mW at a supply voltage of 3.4 V with an efficiency of 0.8, gives us

$$C = \frac{3 \cdot 24 \cdot 0.7066}{3.4 \cdot 0.8} = 18.7 Ah \quad (4.2)$$

The size of the solar cell can be easily estimated if we consider an eight-hour day and a 16-hour night cycle in which the solar panel does not produce energy. As we saw in Figures 2.7 and in 2.8, one can position the panel towards a southern direction with a 30° incline

to get the best efficiency. If 95% efficiency is satisfying, then one can move the solar panel about 45° into western or eastern direction without losing efficiency, see Figure 2.8 again. For the day cycle, all the energy $P = 707$ mW (without GPRS) has to be provided by the solar panel, so

$$W_{day} = P \cdot t \cdot \frac{1}{\eta_{solar}} = P \cdot 8 \cdot \frac{1}{0.95} = 5954 \text{ mWh} \quad (4.3)$$

During the night, all the energy to supply the load has to be provided by the battery. Considering an efficiency of 80% one can calculate

$$W_{night} = P \cdot t \cdot \frac{1}{\eta_{batt}} = P \cdot 16 \cdot 1.25 = 14140 \text{ mWh} \quad (4.4)$$

Adding these two values gives a good estimated value for the necessary peak power of the solar panel:

$$P_{p,solar} = \frac{W_{day} + W_{night}}{8h} = 2512 \text{ mW} \quad (4.5)$$

Connecting the GPRS to the sensor node will result in $P_{p,solar} = 4928$ mW, following the same calculation procedure. Referring to Figure 2.8 again, one can see that during winter the incident global irradiation is about one third of the irradiation during summer. Accordingly, a $15 W_{peak}$ solar panel, the MC-SP15-GCS from Multicomp, has been proposed.

4.1.2 Maximum Power Point Control

Sustaining the system at the maximum power point is crucial for its lifetime. For this purpose, a few algorithms have been selected: Fractional open circuit voltage and the Perturb-Observe algorithm, see section 4.2.3 for the particular implementations. However, with these results the microcontroller can calculate the necessary resistor size for the resistor divider on the IFB pin of the LTC4000-1, which controls the maximum power point.

First the necessary SEPIC converter is calculated in the below-mentioned paragraph [10][32]. The requirements to the converter are the following:

- Minimum input voltage 10 V
- Maximum input voltage 25 V
- Output voltage 14.6 V (absorption voltage of LA battery) and current of 1.2 A
- Switching frequency $f_{sw} = 350$ kHz (easy integration with LTC3786)
- Diode forward loss $V_D = 0.5$ V
- Worst case efficiency of 80%

As always, one first calculates the minimum and maximum duty cycle:

$$D_{min} = \frac{V_{out} + V_D}{V_{in,max} + V_{out} + V_D} = 0.377 \quad (4.6)$$

$$D_{max} = \frac{V_{out} + V_D}{V_{in,min} + V_{out} + V_D} = 0.602 \quad (4.7)$$

Assuming a current ripple of 30%, the peak ripple current I_p through the inductors can be calculated:

$$I_p = I_{out} \cdot \frac{V_{out}}{V_{in,min}} \cdot \frac{30}{100} = 0.523 A \quad (4.8)$$

Now the size of the inductors can be estimated [35], provided that coupled inductors will be used:

$$L_1 = L_2 = \frac{1}{2} \cdot \frac{V_{in,min}}{I_p \cdot f_s} \cdot D_{max} = 16.4 \mu H \quad (4.9)$$

If the I_{rms} and I_{peak} are calculated, an appropriate inductor can be selected. Afterwards, inductor 1 will be the inductor at the input and inductor 2 will present the inductor after the coupling capacitor to ground.

$$I_{rms,inductor1} = \frac{V_{out} \cdot I_{out}}{V_{in,min} \cdot \eta} = 2.19 A \quad (4.10)$$

$$I_{rms,inductor2} = I_{out} = 1.2 A \quad (4.11)$$

$$I_{peak,inductor1} = I_{rms,inductor1} + \frac{1}{2} \cdot I_p = 2.45 A \quad (4.12)$$

$$I_{peak,inductor2} = I_{rms,inductor2} + \frac{1}{2} \cdot I_p = 1.47 A \quad (4.13)$$

The next normative value would be 18 μH . Choosing the MSD1583-183MEB from Coilcraft with 4.3 A saturation current will suit the application. In [32], a calculation is shown where one can determine the temperature rise of the coupled inductor. Due to the lack of temperature coefficients of the inductor manufacturer, this has been bypassed. A fairly low switching frequency, low ripple currents and a big enough housing can avoid this problem though.

Selecting an appropriate power MosFET can be crucial for the lifetime of the converter. Most important parameters are the peak, RMS current and the power loss in the MosFET:

$$I_{peak,MosFET} = I_{peak,inductor1} + I_{peak,inductor2} = 3.92 A \quad (4.14)$$

$$I_{rms,MosFET} = I_{out} \cdot \sqrt{\frac{(V_{in(min)} + V_{out} + V_D) \cdot (V_{out} + V_D)}{V_{in(min)}^2}} = 2.34 A \quad (4.15)$$

$$P_{loss,MosFET} = I_{rms,MosFET}^2 \cdot R_{DS(on)} \cdot D_{max} + (V_{in(min)} + V_{out}) \cdot I_{peak,MosFET} \cdot \frac{Q_{GD} \cdot f_s}{I_G} = 0.504 W \quad (4.16)$$

whereas the power MosFET STD30NF06L from STMicroelectronics in a DPAK package has been selected. This comes with a $R_{DS(on)} = 25 m\Omega$, $Q_{GD} = 10 nC$ and a maximum gate drive current of 0.8 A. The temperature rise of the MosFET in operation can be calculated by multiplying the power losses by the maximum temperature rise coefficient $\Theta_{DPAK} = 100 \frac{^\circ C}{W}$ from the data sheet. Worst case estimation:

$$\Delta T = P_{loss,MosFET} \cdot \Theta_{DPAK} \approx 50 ^\circ C \quad (4.17)$$

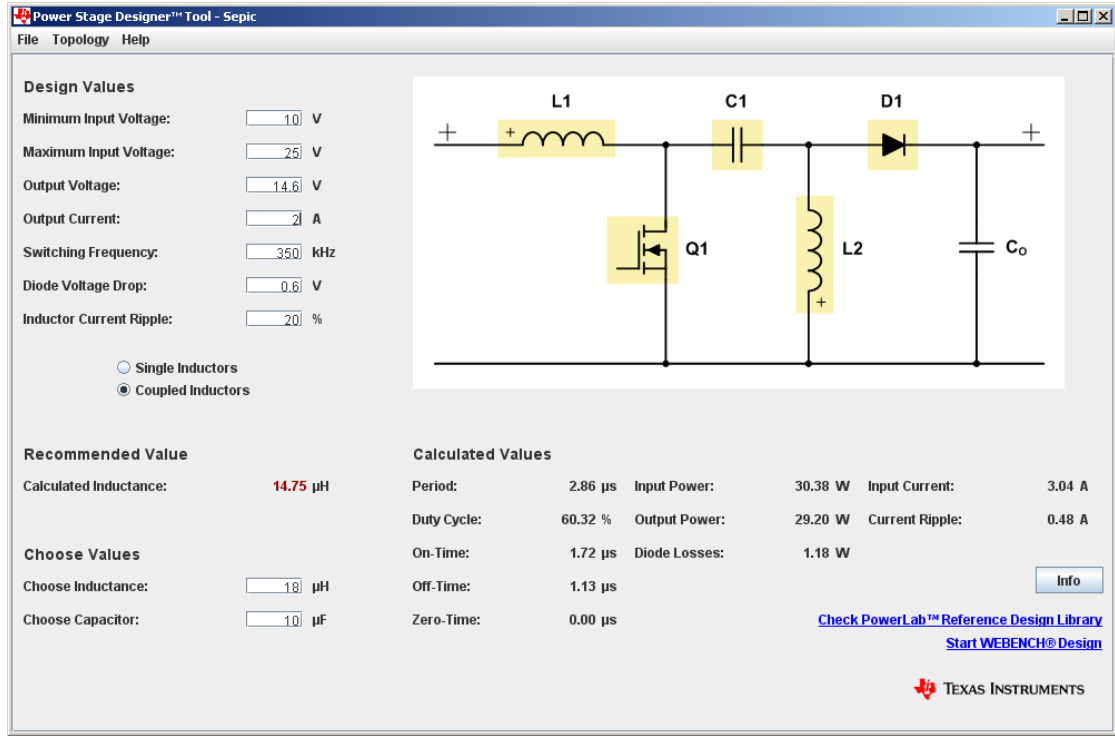


Figure 4.6: Suggested design of the SEPIC converter to track the maximum power point in PowerStageDesigner

The size of the coupling capacitor C_c can be estimated by calculating the RMS current and by selecting the maximum allowed voltage ripple ΔV . In this case, a voltage ripple of $\Delta V = 0.25 \text{ V}$ is supposed:

$$I_{rms,C} = I_{out} \cdot \sqrt{\frac{V_{out} + V_D}{V_{in,min}}} = 1.48 \text{ A} \quad (4.18)$$

$$C_c = \frac{I_{out} \cdot D_{max}}{\Delta V \cdot f_s} = 8.2 \mu\text{F} \quad (4.19)$$

Considering a lower voltage ripple, the coupling capacitor must have a bigger capacity, so $10 \mu\text{F}$ are chosen. The output Schottky diode is selected by adding the maximum input and output voltage:

$$V_{DS} = V_{in,max} + V_{out,max} = 39.6 \text{ V} \quad (4.20)$$

resulting in a 60V Schottky diode. The output capacitor is calculated similarly to the coupling capacitor, so the RMS input current, the ESR and the output voltage ripple will be the interesting factors. Supposing a maximum output voltage ripple of 25 mV:

$$I_{rms,C_{out}} = I_{rms,C} = 1.48 \text{ A} \quad (4.21)$$

$$ESR \leq \frac{\Delta V_{out} \cdot 0.5}{I_{peak,inductor1} + I_{peak,inductor2}} \leq 12.8 \text{ m}\Omega \quad (4.22)$$

$$C_{out} \geq \frac{I_{out} \cdot D_{max}}{\Delta V \cdot f_s \cdot 0.5} \geq 165 \mu F \tag{4.23}$$

Choosing a 220 μF capacitor should even smooth the output voltage more. A comparative design with the PowerStageDesigner from Texas Instruments is presented in Figure 4.6 and the voltage as well as current characteristics in Figure 4.7 to 4.10.

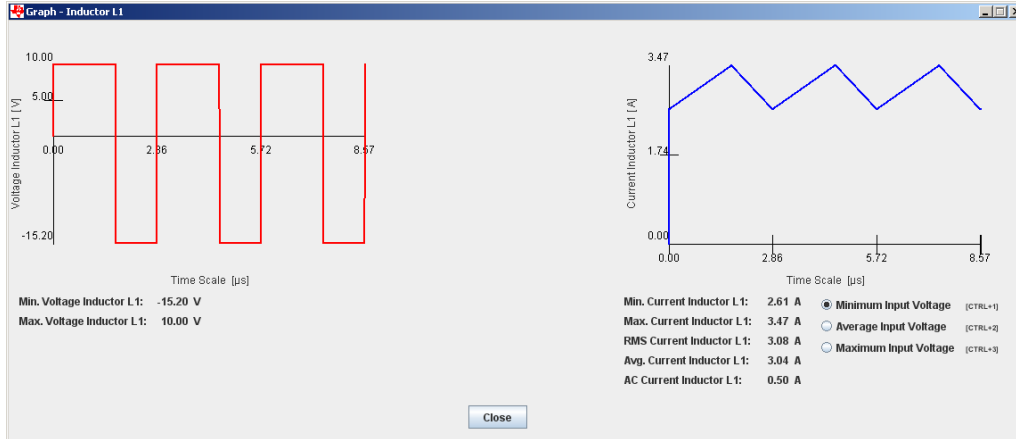


Figure 4.7: Voltage and maximum current characteristic at the primary coil (L1), PowerStageDesigner

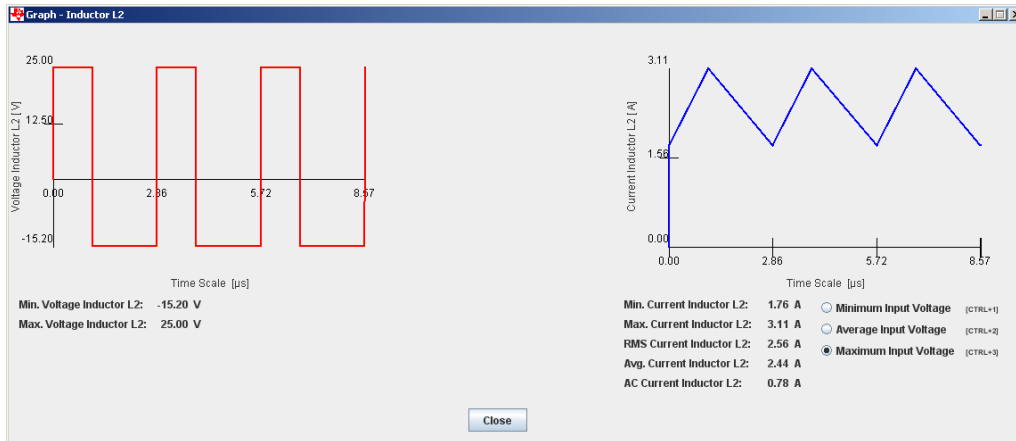


Figure 4.8: Voltage and maximum current characteristic at the secondary coil (L2), PowerStageDesigner

The IFB pin on the LTC4000-1 controls the load on the energy source. Normally, a resistor divider from the input voltage to ground will set the maximum power point voltage to the SEPIC converter. So the LTC4000-1 reduces the load on the source if the voltage on the IFB pin falls below the threshold. One can now set different maximum power points by varying this resistor divider. Two possibilities to change the resistor value would be to (i)

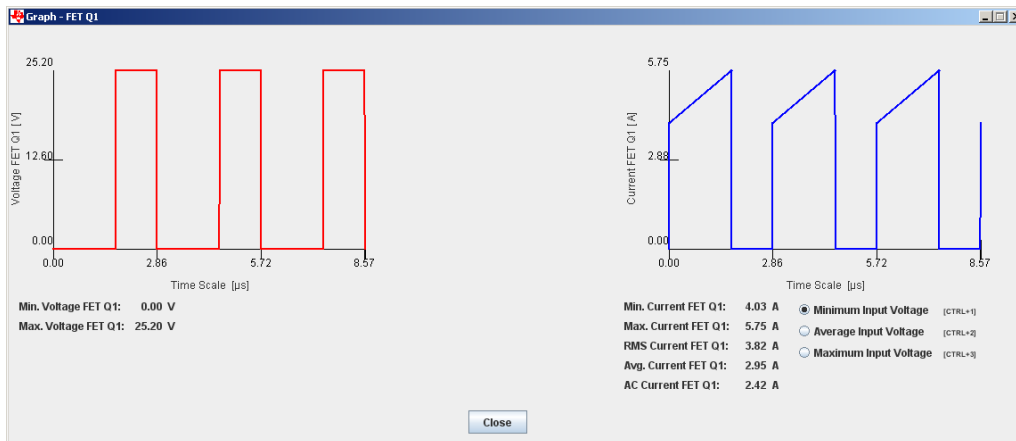


Figure 4.9: Voltage and maximum current characteristic at the n-MosFET (Q1), PowerStageDesigner

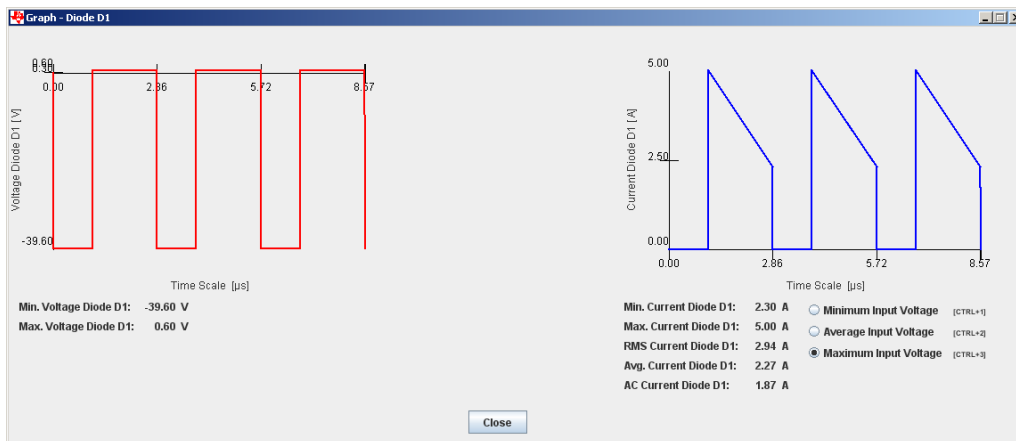


Figure 4.10: Maximum voltage and current characteristic at the Schottky diode (D1), PowerStageDesigner

place a variable resistor in parallel or (ii) get another resistor in series. The role of the variable resistor can be fulfilled with the MCP4152 digital potentiometer.

One problem with the second solution is the case in which the digital potentiometer is not supplied, so a very high ohmic state is assumed. The resistor divider would be somewhat zero and so the voltage on the IFB pin, the LTC4000-1 would not even give the SEPIC converter the command to run. With a resistor in parallel and a p-channel JFET which can be switched off by the microcontroller, this problem can be avoided.

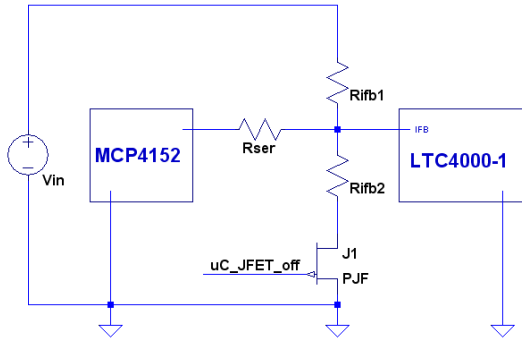


Figure 4.11: Changing the resistor value for MPP tracking in serial mode, complete schematic.

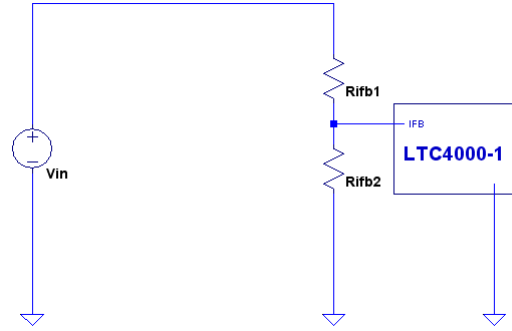


Figure 4.12: In case the digital potentiometer is not supplied, the JFET is turned on and a correct resistor divider is seen on the IFB pin.

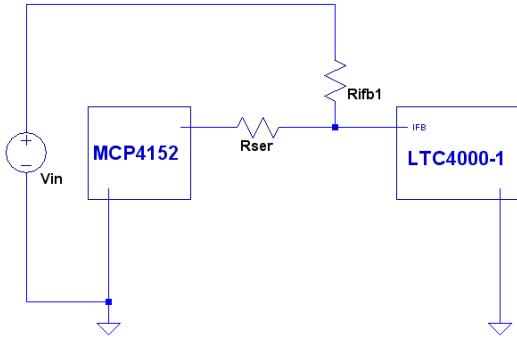


Figure 4.13: In case the digital potentiometer is supplied, the JFET is switched off via the microcontroller and the MCP4152 gives the correct resistor size.

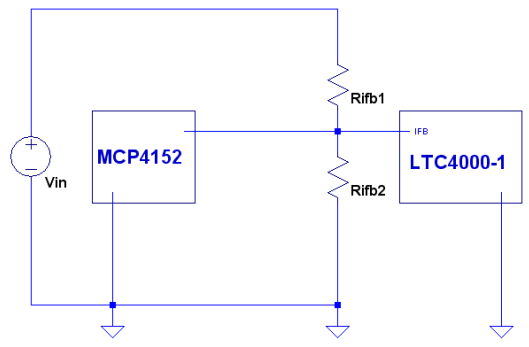


Figure 4.14: Changing the resistor value for MPP tracking in parallel mode

To compare these two methods, the necessary resistor R_{ifb2} depending on the voltage of the maximum power point is calculated:

$$R_{ifb2,needed} = \frac{R_{ifb1}}{V_{MPP} - 1} \quad (4.24)$$

Then, the needed resistor of the digital potentiometer is calculated. For (i)

$$R_{poti,serial} = R_{ifb2,needed} - R_{ser} \quad (4.25)$$

and (ii)

$$R_{poti,parallel} = \frac{R_{ifb2} \cdot R_{ifb2,needed}}{R_{ifb2} - R_{ifb2,needed}} \quad (4.26)$$

For the serial method, a combination of a serial resistor and the MCP4152 has been chosen, which has a $p_{serial} = 5\text{ k}$ variable resistor range and $r = 8$ bit resolution. The parallel method would not need a serial resistor, but would need a variable $p_{parallel} =$

100 k Ω resistor range with the same resolution. Now we can calculate the code on the digital potentiometer and the resolution of the method:

$$Code = \left(\frac{R_{poti,serial}}{p_{serial}} \right) \cdot 2^r \quad (4.27)$$

$$Resolution = \frac{\log(\Delta Code)}{\log(2)} \quad (4.28)$$

A comparison of the bit resolution of these methods is shown in Table 4.1. For this purpose, the resistors R_{ifb2} and R_{ser} have been chosen to be 47 k Ω and 1.5 k Ω . As one can obtain the resolution for the serial method is much higher than for the parallel method. So the serial version is preferred.

Table 4.1: Comparison of the serial and parallel methods to control the MPP. V_{MPP} is the voltage of the maximum power point, $R_{ifb2,needed}$ is the needed resistor to form the correct resistor divider to the IFB pin and the resolutions are given in bits.

V_{MPP} [v]	$R_{ifb2,needed}$ [Ω]	Resolution serial	Resolution parallel
10	5222	-	-
11	4700	4	4
12	4273	4	3
13	3917	4	2
14	3615	3	2
15	3357	3	1
16	3133	3	1
17	2937	3	1
18	2764	3	0
19	2611	3	0
20	2473	2	0

4.1.3 Reverse Current Mode Control

The reverse current mode is best served with an LED driver that drives the desired output current to the solar cell. A few designs had been reviewed and all of the LED drivers had one drawback in common. The output current is controlled by comparing the sense voltage to an internal signal. This sense resistor will give a constant power loss of a few hundred mW because it will always be connected to the solar cell indifferent whether the reverse current mode is active or not. A first approach to feed a μC controlled PWM voltage to the Micrel 3223 resulted in a burned IC. The control with the used μC was too slow and, therefore, resulted in a very high current.

Similarly to MPP tracking, a SEPIC converter is the best solution in this case and can avoid the mentioned problem. This type has been chosen to effectively disconnect the output from the input while still having a higher efficiency than the presented LED driver. In the design, the LM3488 SEPIC controller with an external switch from Texas Instruments is used. The requirements to the converter are the following:

- Minimum input voltage 10.5 V (end of life of battery)
- Maximum input voltage 13.5 V (end of charge voltage of battery)
- Output voltage 26 V and output current 0.9 A
- Switching frequency $f_{sw} = 480$ kHz (determined by microcontroller)

The application note AN-1484 from Texas Instruments gives a good introduction into the design of SEPIC DC/DC converters in combination with the LM3488 and was used to estimate the component values for the reverse current mode. Assuming the worst case for the Schottky diode (MBRS360T3) of 0.4 V, one can calculate the necessary maximum and minimum duty cycle of the gate PWM signal:

$$D_{min} = \frac{V_{out} + V_D}{V_{in(max)} + V_{out} + V_D} = 0.64 \quad (4.29)$$

$$D_{max} = \frac{V_{out} + V_D}{V_{in(min)} + V_{out} + V_D} = 0.72 \quad (4.30)$$

To get a lower input inductor current ripple, 20% ripple current is chosen:

$$\Delta I_L = I_{out} \cdot \frac{V_{out}}{V_{in(min)}} \cdot \frac{20}{100} = 0.482 \text{ A} \quad (4.31)$$

There are two possible ways of inductor use for SEPIC converters. On the one hand one can use a coupled inductor and on the other hand one can use two distinct inductors which will result in higher inductance values. Comparing the voltage and current waveforms when used in SEPIC design will give very similar results, so which one is better? [35][36] tried to address this concern.

Merely the high off-the-shelf variety of single inductor can be sufficient. Coupled inductors persuade with reduced component count, more feasible integration and lower inductance requirements. This may be true for standard designs, but designing more complex power regulators often results in non-availability of coupled inductors with certain characteristics, leading to design-appropriate inductors. However, in [35], coupled inductors had been designed nevertheless single inductors came with huge instabilities in the control loop of the converter. Resolving this issue resulted in an even higher amount of components and size on the board. Given that the outcome is pretty much the same, coupled inductors are preferred.

In this design coupled inductors are used, so one can determine the size of a single inductor

$$L_1 = L_2 = \frac{V_{in(min)}}{\Delta I_L \cdot f_{sw}} \cdot D_{max} = 31.81 \mu H \quad (4.32)$$

and approximately halve this value [35]. The limiting factor is the current rating which can be estimated with the peak current through the inductor L_1 at the input:

$$I_{L1(peak)} = I_{out} \cdot \frac{V_{out} + V_D}{V_{in(min)}} \cdot \left(1 + \frac{0.2}{2}\right) = 2.69 \text{ A} \quad (4.33)$$

The coupled inductor MSD1583 with 18 μH and a current rating of 4.3 A has been chosen. The output diode must withstand a reverse voltage $V_{in(max)} + V_{out} = 39\text{ V}$ and an average diode current equal to the output current at full load. For this purpose, the MBRS360T3 fulfils all requirements perfectly.

A very important part in this type of converters is the power MosFET and has to be chosen very carefully. The MosFET peak current is just the sum of the peak currents of the inductors and results in 3.8 A. The effective RMS current is calculated via

$$I_{RMS} = I_{out} \cdot \sqrt{\frac{(V_{in(min)} + V_{out} + V_D) \cdot (V_{out} + V_D)}{V_{in(min)}^2}} = 2.9\text{ A} \quad (4.34)$$

The gate drive current I_G is 0.3 A for the LM3488, so one can now estimate the power losses. The drain-source voltage must withstand $V_{in(max)} + V_{out} = 39\text{ V}$ and a maximum power dissipation of

$$P_{loss} = I_{RMS}^2 \cdot R_{DS(on)} \cdot D_{max} + (V_{in(min)} + V_{out}) \cdot I_{peak} \cdot \frac{Q_{GD} \cdot f_{sw}}{I_G} = 1.025\text{ W} \quad (4.35)$$

The power MosFET SQ4850EY in a SOIC-8 case has been chosen.

The screenshot shows the Power Stage Designer tool interface for a Sepic converter. The design values are as follows:

Design Values	Value
Minimum Input Voltage:	10.8 V
Maximum Input Voltage:	13.5 V
Output Voltage:	26 V
Output Current:	1 A
Switching Frequency:	500 kHz
Diode Voltage Drop:	0.4 V
Inductor Current Ripple:	20 %

The circuit diagram shows a Sepic converter with components L1, C1, D1, Q1, L2, and Co. The inductor L1 is highlighted in yellow.

The Recommended Value section shows:

Recommended Value	Value
Calculated Inductance:	15.92 μH

The Calculated Values section shows:

Calculated Values	Value
Period:	2.00 μs
Duty Cycle:	70.97 %
On-Time:	1.42 μs
Off-Time:	0.58 μs
Zero-Time:	0.00 μs
Input Power:	26.37 W
Output Power:	26.00 W
Diode Losses:	0.37 W
Input Current:	2.44 A
Current Ripple:	0.77 A

The Choose Values section shows:

Choose Values	Value
Choose Inductance:	<input type="text"/> μH
Choose Capacitor:	<input type="text"/> μF

The interface also includes a menu bar (File, Topology, Help), a status bar (Texas Instruments), and links to PowerLab Reference Design Library and WEBENCH Design.

Figure 4.15: Suggested design of the reverse current mode in PowerStageDesigner

The last part to design is/are the output capacitor(s):

$$C_{out} \approx \frac{I_{out} \cdot D_{max}}{V_{ripple} \cdot 0.5 \cdot f_{sw}} = 10.93 \mu F \quad (4.36)$$

whereas V_{ripple} is assumed to be 1% of the output voltage. Putting three 10 μF ceramic capacitors in parallel should be enough.

During the design process a few utile programmes like the PowerStageDesigner from Texas Instruments or the webpage of coilcraft could be used to verify the design. A few results are shown in Figures 4.15 to 4.19.

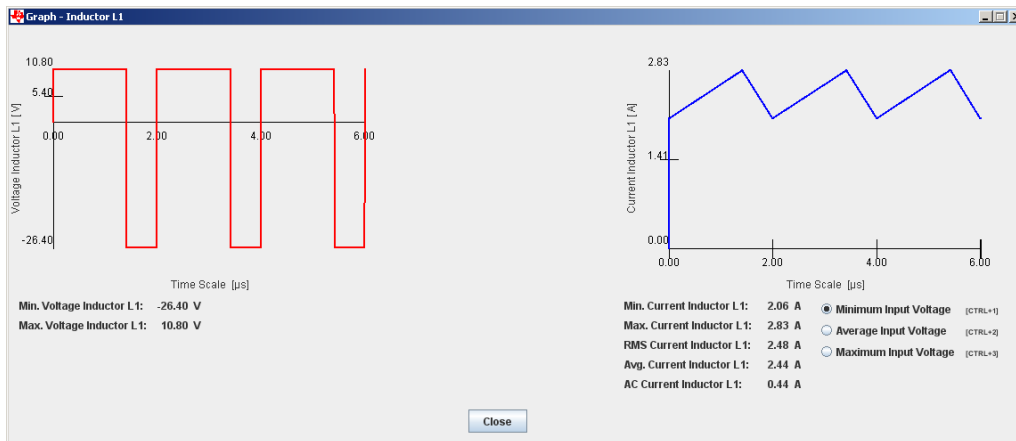


Figure 4.16: Voltage and maximum current characteristic at the primary coil (L1), PowerStageDesigner

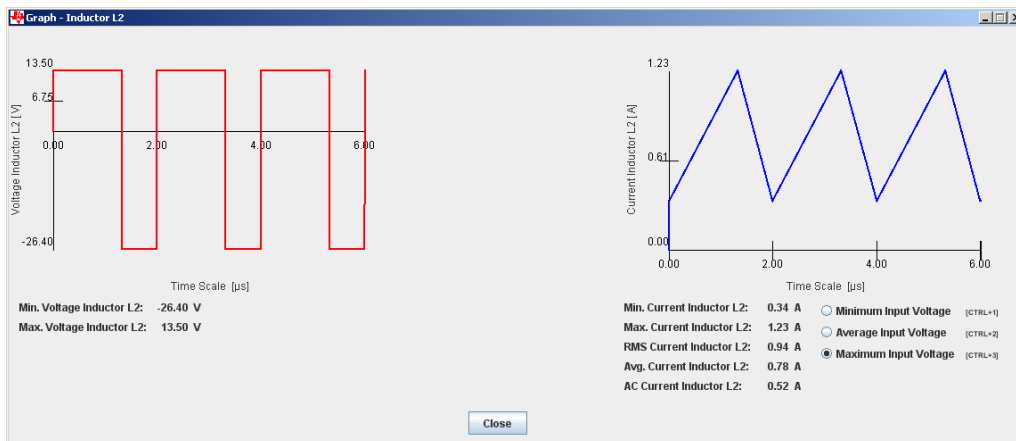


Figure 4.17: Voltage and maximum current characteristic at the secondary coil (L2), PowerStageDesigner

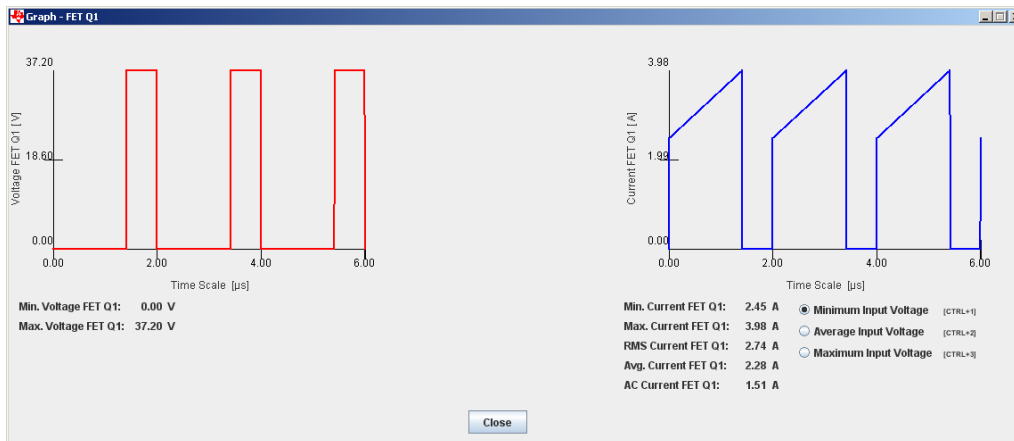


Figure 4.18: Voltage and maximum current characteristic at the n-MosFET (Q1), PowerStageDesigner

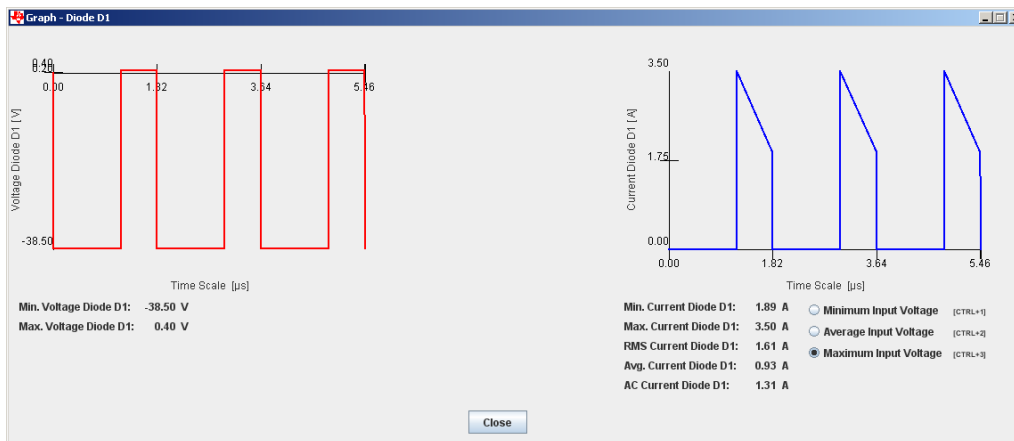


Figure 4.19: Maximum voltage and current characteristic at the Schottky diode (D1), PowerStageDesigner

4.1.4 Battery Charging

In the second chapter Table 2.1, there is an overview of applicable batteries given. Considering harsh environments and the temperature range, only calcium-based and lead acid batteries can be used. Calcium-based batteries are much cheaper than lead acid batteries, resulting in ≈ 20 Euro per 65 Ah. A few problems arise when using calcium-based batteries. First, they have to be charged with at least 15.8 to 16 V with maximum current of one tenth of the rated capacity, whereas for a 65 Ah battery a current of 6.5 A would be needed [26]. Second, one would need a special charging programme to fully recover and, finally, if the voltage level is lower than 15.8 V while charging, a phenomenon called acid layering will occur. This effects the stirring of the electrolyte resulting in different acid

layers in the battery cells. Lead acid batteries are easier to handle and also more resistant to this phenomenon.

For the purpose of charging a lead acid battery, there exist a wide variety of charging-integrated circuits (ICs). The possibility to simulate the charging component, the wide input voltage range and to operate the whole system in MPP despite charging the battery led to use of the LTC4000 from Linear Technologies. This high voltage high current battery management controller had only one problem: The charging occurred in stop and go mode, means charging until it reached a given voltage then it shut down until the voltage at the battery reached a lower limit. Reaching the lower limit restarted the charging process. During the design process, Linear Technology launched the successor LTC4000-1 where charging became much simpler. With this IC it is also possible to run through different charging steps. Furthermore, the charging current and different charging modes can be selected.

The first mode is to place a capacitor from the TMR pin to the ground which will enable the timer mode. The size of the capacitor will determine the duration of the charging cycle. This mode is only reasonable when using a permanent energy supply. Constant charging is enabled by connecting the TMR pin directly to the ground and is the second mode. Charging stops when the CHR# pin is pulled high. The last mode demands that one connects the TMR pin to the BIAS pin so that charging terminates when the charge current I_{cx} drops below the limit one sets by placing a resistor from the C/X pin to ground. The second mode has been selected due to the possibility of controlling the charging process with the MCU.

The LTC4000-1 offers the possibility of observing the input current as well as the battery charge current through the IIMON and IBMON pins. A 10 nF capacitor is placed, so the capacitor voltage is 20 times the sensed voltage across the sense resistors.

Another feature is the undervoltage lockout. The necessary resistors can be selected through the VM pin and the relation

$$V_{VM} = \frac{R_{VM,1} + R_{VM,2}}{R_{VM,2}} \cdot 1.193 \quad (4.37)$$

$R_{VM,1}$ was chosen to be 100 k Ω , so $R_{VM,2}$ equals 21.5 k Ω . A parallel zener diode to limit the maximum input voltage to 2 V of the Schmitt Trigger is needed. This zener diode has been replaced with three silicon 1n4148 diodes due to the lower noise current.

Observation of the charge current is of great importance. Two pins are defined for this purpose. On the one hand there is the CL pin which limits the maximum current into the battery. Leaving this pin open results in a maximum charging current of:

$$I_{CL} = \frac{50mV}{R_{cs}} = \frac{50mV}{33m\Omega} = 1.512 A \quad (4.38)$$

On the other hand, the CX pin sets the limit for the minimum charge current where the IC switches the charging procedure off:

$$I_{cx} = \frac{0.25\mu A \cdot R_{cx} - 0.5mV}{R_{cs}} \quad (4.39)$$

Whereas I_{cx} is supposed to be ≈ 70 mA and the sense resistor R_{cs} equals 33 m Ω . This results in a resistor value of $R_{cx} = 10$ k Ω .

The charger can be set or unset with the ENC pin. Pulling the pin low shuts off the charging procedure. It can be started again by pulling the pin high. In our case this is not necessary because the LTC4000-1 can shut down the charging procedure via the I_{th} and CC pin with the interconnections to the DC/DC converter. One still needs to control the RST# to shut down all components which is done with the MCU and a transistor. The CHRG# pin serves as an interrupt flag to the μC so one knows when the charging procedure is finalized. If the pin is high, then charging has been terminated. Charging normally pulls this pin down to low.

The load switch at the IGATE pin is selected depending on the maximum load current, the power dissipation and the reverse voltage drop. Furthermore, a low gate capacity will increase switching speed. The IRLML9301 PMOS of International Rectifier (IR) has been chosen due to its necessary low gate charge, high drain source and gate source voltage while keeping the on state resistance low. A Gate-Source Voltage of 15 V is needed due to the maximum value of $V_{IGATE(on)}$.

The battery management of the LTC4000-1 is capable of controlling a DC/DC converter via the I_{th} and CC pin. If one sets the voltage levels at the FBG, BFB and BAT correctly, one can adopt the implemented three-stage charging process. Setting the absorption and float voltage will bring the desired charging behaviour:

$$V_{float} = \left(\frac{R_{BFB1}}{R_{BFB2}} + 1 \right) \cdot 1.136 = 13.55 \text{ V} \quad (4.40)$$

where the resistors had been chosen to $R_{BFB1} = 390 \text{ k}\Omega$ and $R_{BFB2} = 35.7 \text{ k}\Omega$. For the absorption voltage one needs to choose R_{BFB3} , in this case $523 \text{ k}\Omega$.

$$V_{absorption} = \left(\frac{R_{BFB1} \cdot (R_{BFB2} + R_{BFB3})}{R_{BFB2} \cdot R_{BFB3}} + 1 \right) \cdot 1.136 = 14.5 \text{ V} \quad (4.41)$$

Few pins have a comparator and a following amplifier with a limited bandwidth and non-linearity. A filter network on the I_{th} and CC pin is required, which is really difficult to determine. Simulations in LTSpice with the desired arrangement showed good compliance with $R_{th} = 28.7 \text{ k}\Omega$ and $C_C = 22 \text{ nF}$.

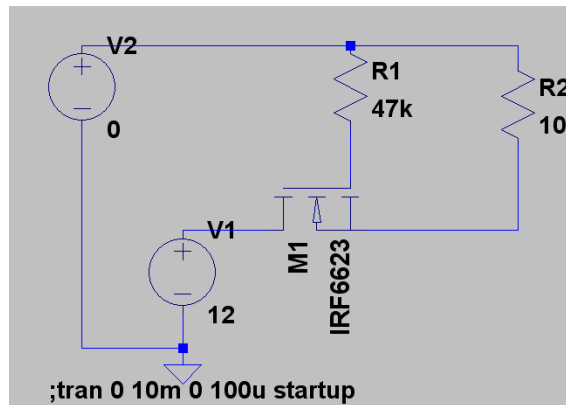


Figure 4.20: Reverse polarity protection for the lead acid battery, simulated in LTSpice.

To protect the system in case of an incorrectly connected battery, a reverse polarity protection is integrated. As long as the battery is plugged in correctly, the system works properly. If the battery is plugged in in reverse, the drain source voltage will be lower than the gate source voltage, so the NMOS will not switch on and therefore the ground is disconnected. The resistor connected to the gate will reduce the power loss through the NMOS. The schematic is represented in Figure 4.20.

4.1.5 Current and Voltage Measurement

By measuring the input and the output current and voltage one can define the actual state of the system. Whereas the voltage can be easily measured with an ADC unit on the MCU, the current measurement is more complicated. For this purpose a current-shunt monitor INA214 from Texas Instruments is used. This shunt monitor allows not only to measure the current, it is also possible to make a statement about the direction of the electric current.

This is needed at the input of the photovoltaic cell to measure the incoming current and also to measure the current when operating in reverse current mode. Setting the zero level of the REF pin gives values from zero to the zero level when current flows from one direction to the other and voltage levels from the REF level to the supply voltage for current flowing in the other direction. To avoid high power losses on the shunt resistor, a built-in internal amplification amplifies the measured voltage in the case of the INA214 by a factor of 100. To get the same result in both directions, a resistor divider with same size resistors and a following buffer is used. If one wants a maximum output signal of 3.3 V and a theoretically measured maximum current of 1 A, the sense resistor value will hold:

$$R = \frac{U}{I \cdot V} = \frac{3.3}{1 \cdot 100} = 33 \text{ m}\Omega \quad (4.42)$$

Same is valid for measurements in both directions:

$$R = \frac{U}{I \cdot V} = \frac{1.65}{1 \cdot 100} = 16.5 \text{ m}\Omega \quad (4.43)$$

Due to the non-availability of 16.5 m Ω a 15 m Ω resistor has been chosen. Because of deployment of the INA214 near the battery and the reverse current power regulator, there is a high possibility of common-mode transients that can harm the shunt monitors. For this purpose 10 Ω resistors and small Schottky diodes are used for prevention.

4.1.6 Power Supply

In [16] a voltage level of 3.4 V and a maximum current of 320 mA is needed. For this demand a Power Buck converter is used. In this case one cannot use charge pumps because of the possible low output current.

The LM22672 simple switcher of LT for step down converters is chosen. Its high voltage input range, the high possible output current of 1 A and the integrated MosFET with adjustable switching frequency suits our needs perfectly. This module comes in the adjustable and the fixed 5 V versions. In our case the adjustable mode was selected. To begin, the feedback divider has to be set:

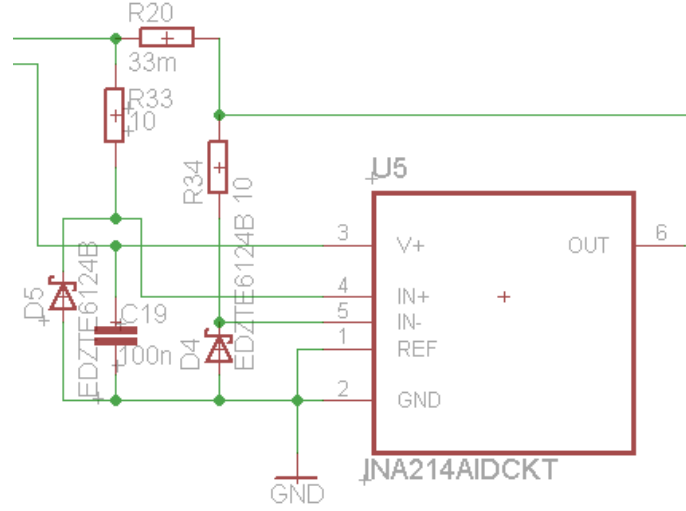


Figure 4.21: Transient protection of a current-shunt monitor using a resistor in series with a zener diode

$$R_1 = \frac{R_2}{\frac{V_{out}}{V_{FB}} - 1} \quad (4.44)$$

whereas the output voltage V_{out} is chosen to be 3.4 V according to [16] and the feedback voltage V_{FB} is pre-set to 1.285 V. Choosing R_2 to be 5100Ω, states

$$R_1 = 3089.2 \Omega \quad (4.45)$$

A resistance value of 3090 Ω is chosen. Setting the switching frequency determines the size of the inductor. In general, a small PCB design is preferred, so a higher switching frequency is needed. In case of the LM22672, an external resistor is used to set the frequency. Preferring a switching frequency of 750 kHz needs a resistor of approximately 47 kΩ. Keeping in mind that the maximum peak current that can be delivered by the module before it reaches the overload condition is 1.5 A, the inductor size L can be chosen according to

$$L = \frac{V_{out} \cdot (V_{in(max)} - V_{out})}{I_{ripple} \cdot f_{sw} \cdot V_{in(max)}} \quad (4.46)$$

whereas the following values have been considered: $V_{out} = 3.4$ V, $V_{in(max)} = 23$ V, $f_{sw} = 750$ kHz and I_{ripple} to be about 40% of the maximum output current of 500 mA.

$$L = 20.12 \mu H \quad (4.47)$$

An inductor size of 22 μH has been chosen. For proper functionality a bootstrap capacitor, a catch diode and an appropriate output capacitor have to be selected. A 10 nF, low ESR ceramic capacitor is sufficient for the bootstrap capacitor. The catch diode should be a Schottky diode and not be an ultra-fast diode due to the reverse recovery current transients

that will damage the module. The reverse breakdown voltage rating should be 1.5 times higher than the maximum input voltage. This will result in about 34 volts, so a Schottky diode MBRS340T3 with a reverse voltage rating of 40 V was selected. The size of the output capacitor can be estimated based on the voltage ripple

$$\Delta V_{out} = I_{ripple} \cdot \left(ESR + \frac{1}{8 \cdot f_{sw} \cdot C_{out}} \right) \quad (4.48)$$

I_{ripple} , f_{sw} selected as before and trying to regulate ΔV_{out} to be approximately 1mV, an output capacitor of 44 μF is needed. Two 22 μF low ESR ceramic capacitors are put in parallel.

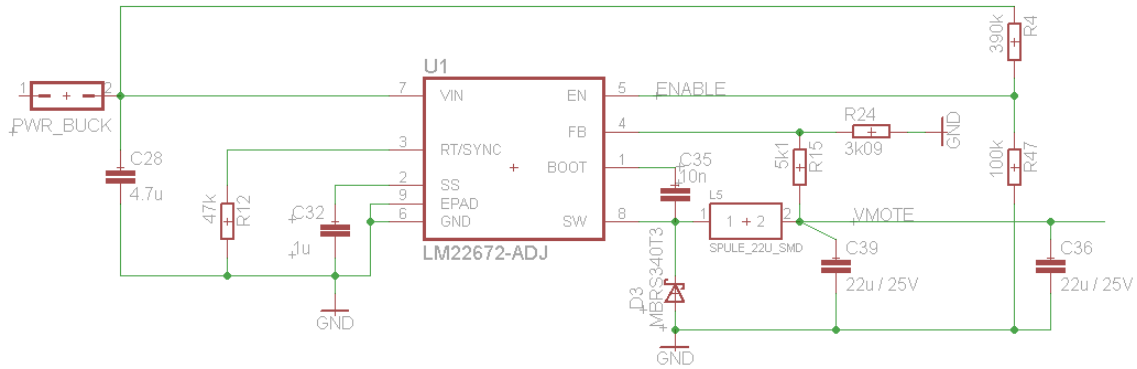


Figure 4.22: Design of the 3.4 V power supply to the sensor node

4.2 Software

The control of the EHS follows the program flow presented in 4.23. This is done when powering up or after a reset has occurred. After stopping the Watchdog Timer, all components are initialized. Switching off the reverse current mode is crucial to normal operation. Afterwards,

- the input current and voltage
- the output current and voltage

are measured and the respective power values are calculated. The light intensity value, that is obtained via the I2C interface from the sensor node, can be used in the calculation of the MPPT algorithm. The maximum power point can be estimated with the fractional open circuit or rather the Perturb and Observe algorithm. The evaluated resistor size is then set via the digital potentiometer over SPI.

Afterwards the MCU is set in a low power mode which will in this case be LPM0 and is waiting for an interrupt which will bring up the MCU again. Interrupts can occur through activating the reverse current mode to de-ice the solar cell, via the communication with the sensor node over I2C [34] as well as timed.

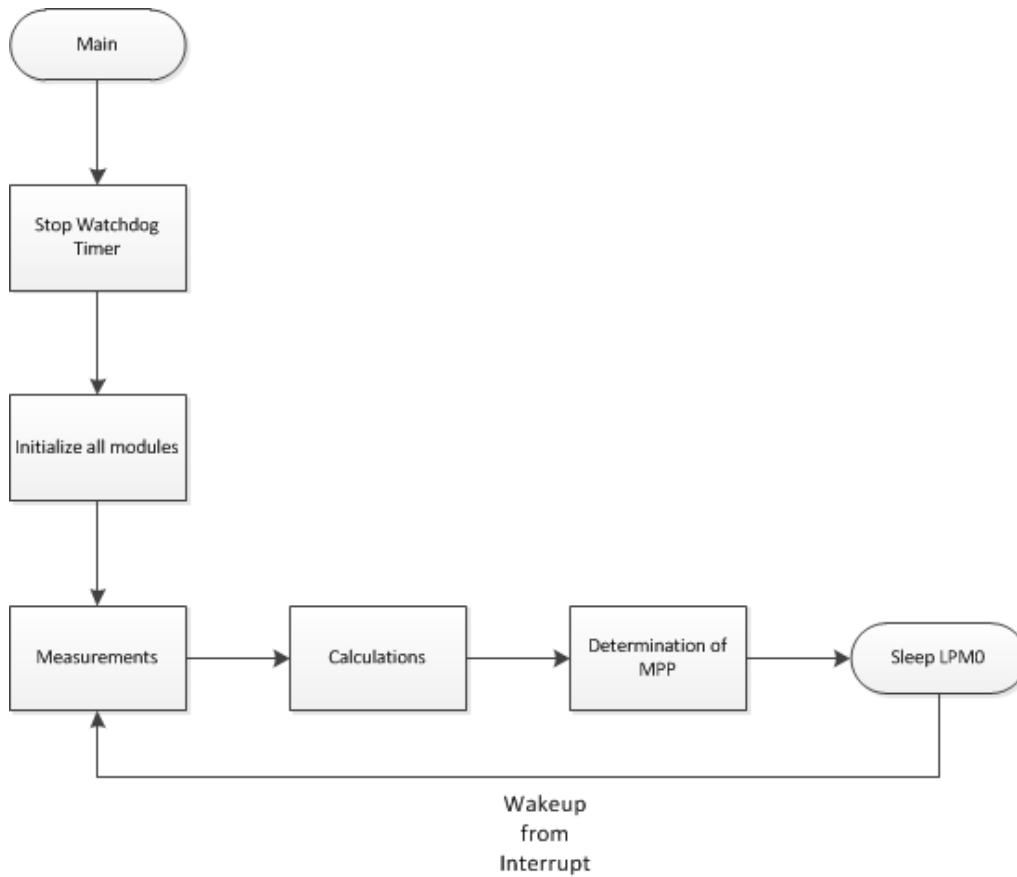


Figure 4.23: Sequence flow of the EHS programme

4.2.1 Interrupt Service Routines

Furthermore, the software includes interrupt handling. Interrupts can be triggered within ADC, Port, Timer and I2C operation. Whereas the operation of the ADC is described in the user guide of Texas Instruments for the MSP430F2274, the sequence diagram of the Port Interrupt Service Routine are presented in Figure 4.24. Pin 3 is used to detect the end of the charging procedure, so the microcontroller can send the status information to the I2C master. In case more than one interrupts occur simultaneously, a proper service routine is implemented. The I2C communication is controlled by the I2C Master which is in our case the microcontroller in the sensor node design [34]. The MSP430F2274 used in the EHS design has to be initialized as Slave, given an address and it also needs to know which pins are used for I2C communication.

4.2.2 Reverse Current Mode (RCM)

To use the reverse current mode it is important to switch off the SEPIC converter at the input. For this purpose, the converter is switched into open circuit configuration which can be easily done by deactivating the charging IC and, therefore, setting the compensation

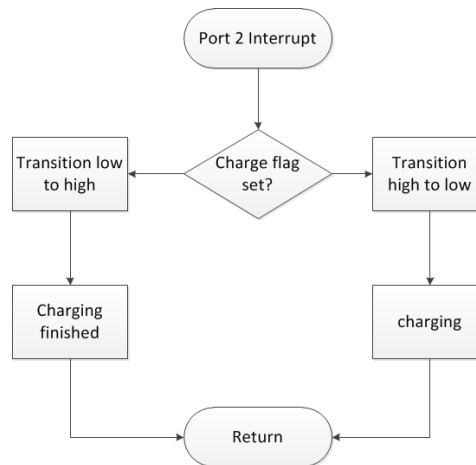


Figure 4.24: Sequence diagram of the Port Interrupt Service Routine for different cases

for the converter. The RCM can now be activated with the pulse width modulated signal of the microcontroller. A high pulse with a width of more than $30 \mu\text{s}$ stops the RCM and the charging IC is again activated.

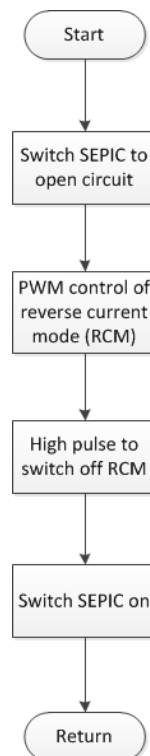


Figure 4.25: Sequence diagram of the Reverse Current Mode (RCM)

4.2.3 MPP Tracking Algorithms

Fractional Open Circuit ... In this case the SEPIC converter is switched into open circuit and the input voltage is measured. The open circuit state can be achieved by setting the reset# connection to ground level. Multiplying the input voltage value with a constant factor α will give us the momentary MPP. Assuming room temperature of 25° , an open circuit voltage of the solar cell of 21.5 V and a MPP at these conditions of 17 V, α will be 0.7907

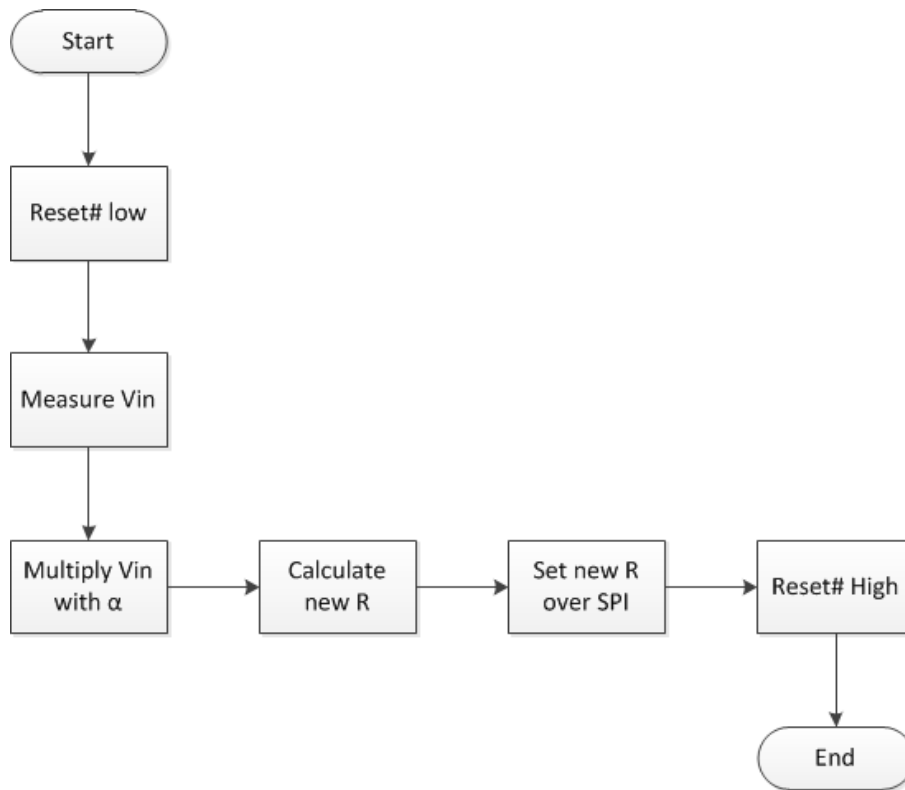


Figure 4.26: Sequence diagram of the Fractional Open Circuit control algorithm

Perturb and Observe ... The idea is to perturb the input and observe the output. Measuring U-I values at the input and the output will give the power values. Changing the momentary resistor size to control the voltage at the maximum power point by a somewhat small positive ΔR , will change the obtained power at the output. Increases the power, ΔR will be positive in the next step too. A decrease results in a negative ΔR . A problem could arise with oscillating behaviour around the MPP.

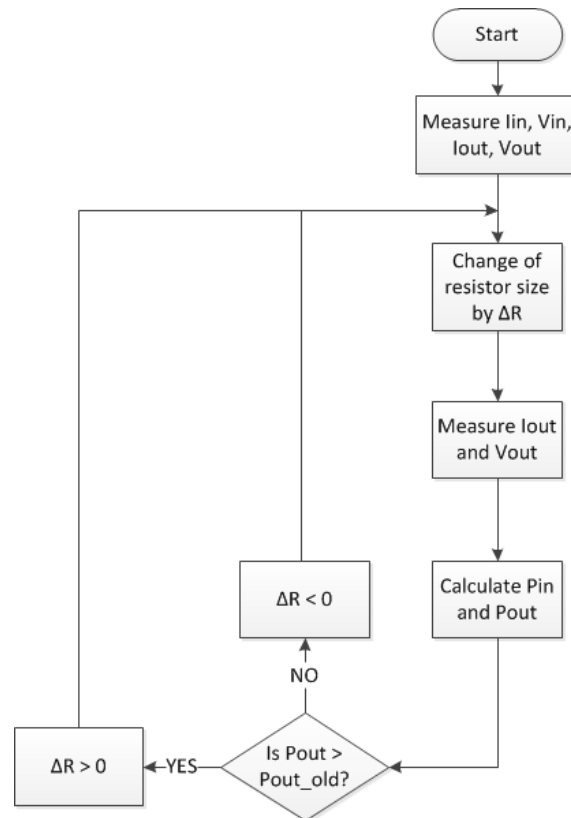


Figure 4.27: Sequence diagram of the Perturb and Observe algorithm

4.2.4 Implementation

Single hardware units are handled in separate classes:

Ports: Defines the signal directions and the interfaces

Crystal: Sets the oscillating frequency for the master and submaster clock

Timer: Controls the PWM signals and counters

RWB: Reverse Current Mode (RCM)

I2C: Controls the I2C interface and therefore the communication with the sensor node

SPI: Controls the SPI interface to set the wiper on the digital potentiometer

ADC: Reads voltage signals and converts them into 10-bit integer values

MPPT: Implements different MPP tracking algorithms

Figure 4.28 shows the possible interactions between the processes.

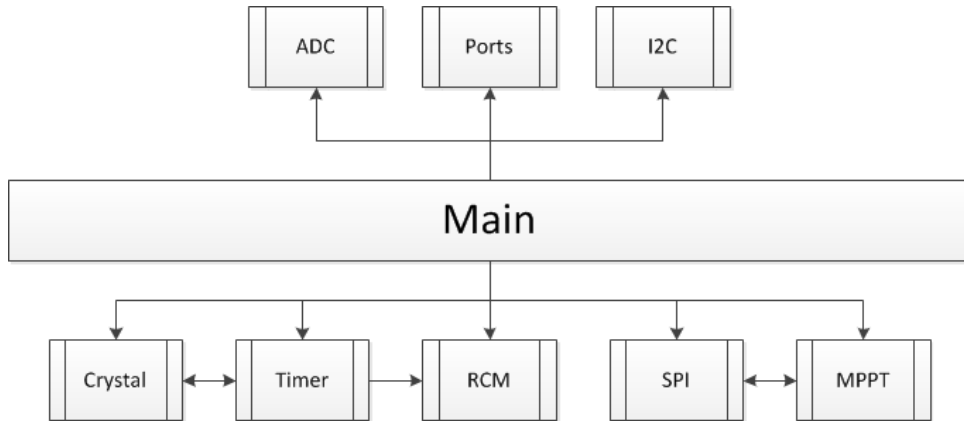


Figure 4.28: Overview of the connections between single processes

4.3 Mounting

An IP67 case has been chosen to fit all the requirements for the mounting. The Fibox PCM95T is 230 mm x 140 mm in size and has a clear cap, so it is possible to mount the light sensor inside the case. Spacer bolts are attached to the bottom of the case, allowing the GPS module to be placed between them. On top of these spacer bolts, an acrylic glass serves as a mounting pad for the energy harvesting device and the sensor node with all of its expansions.

The EHS and the sensor node are connected with four wires which also allows the I2C communication. The solar cell and the battery are connected with the EHS and the wires are lead through WISKA screw connectors.

External sensors or antennas like the one for GPS or radio are connected either to a 4-pole DIN plug or are realized with WISKA screw connectors. The advantage of these screw connectors is quite obvious with the possible lead through and the IP-68 lock just by tightening the screw.

Finally, the whole case is mounted on a grounded iron rod with the GPS antenna on top.



Figure 4.29: A barebone case with already drilled sensor connectors.



Figure 4.30: Including a GPS receiver and a sensor node mounted on plexiglass.



Figure 4.31: A sealed sensor node with harvesting system in case.



Figure 4.32: Complete system mounted on a rod with connected battery and GPS antenna. Test carried out in Wald am Schoberpass, Styria.

4.4 Conclusion

In this chapter the implementation of an energy harvesting system has been presented. The software for the MSP430F2274 microcontroller is written in C in a development kit called the Code Composer Studio. The hardware units are handled in separate classes and follow the programme flow shown in 4.23. For calculation of the MPP, the input and output currents are measured with INA214 current shunt monitors whereas the input and output voltages are digitalized with ADCs of the MCU. Depending on the outcome of an MPPT algorithm, the calculated power values will give an idea if the system is in its MPP or not. To keep the system in its MPP, a variable resistor is set to reduce / increase the load on the energy source.

The system can be switched into a reverse current mode to de-ice a solar cell that is used to harvest energy. For this purpose, a SEPIC converter with coupled inductors is used. The size of this solar cell should be 15 W peak and is calculated in 4.1.1. During winter the system is kept alive by a combination of the solar cell and a battery, whose size is also calculated in 4.1.1. A thermoelectric generator will not be used due to its very low efficiency, see also [31].

The supply for the sensor node is accomplished with the LM22672 from LTC and delivers 3.4 V. Communication between the EHS and the sensor node is accomplished via the I2C interface. Whereas the EHS delivers status information like SOC of the battery, charging status or which energy sources are in use at the sensor node, it gets in return the light intensity and the surrounding temperature value.

Finally the sensor node and the energy harvesting system are mounted in an IP-68 case. Connectors for each antenna and for the sensors are lead-through.

Chapter 5

Results

In this chapter the obtained experimental results are reviewed and compared to the simulations that had been carried out in LTSpice, TinaTI and PSpice.

5.1 Energy Source

In case of the GeoWSN project, a solar cell and a battery have been chosen as energy sources. The solar cell is characterized with diodes and a current source. This model is widely used and the simulation is represented in Figures 5.1 - 5.2

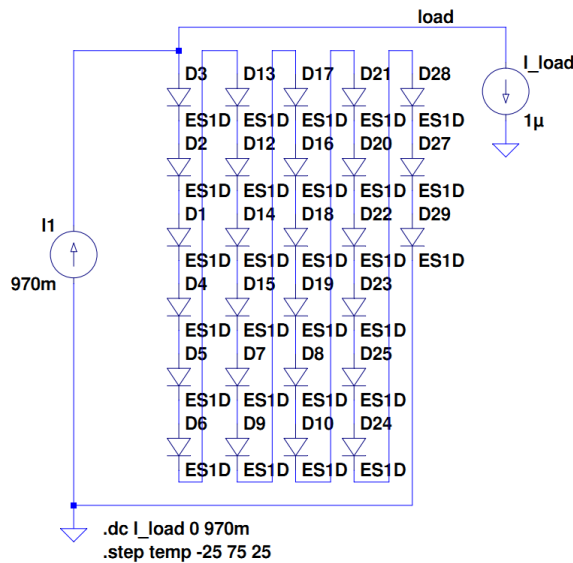


Figure 5.1: Schematic representation of a solar cell with diodes and a current source.

A characterization of the used solar cell has been made upon a measurement board [33]. With these settings one can observe the typical UI-characteristic curve and the output power over the day. The placement of the solar cell and the measurement had been done on a balcony, directed to the north so the output power was relatively low.

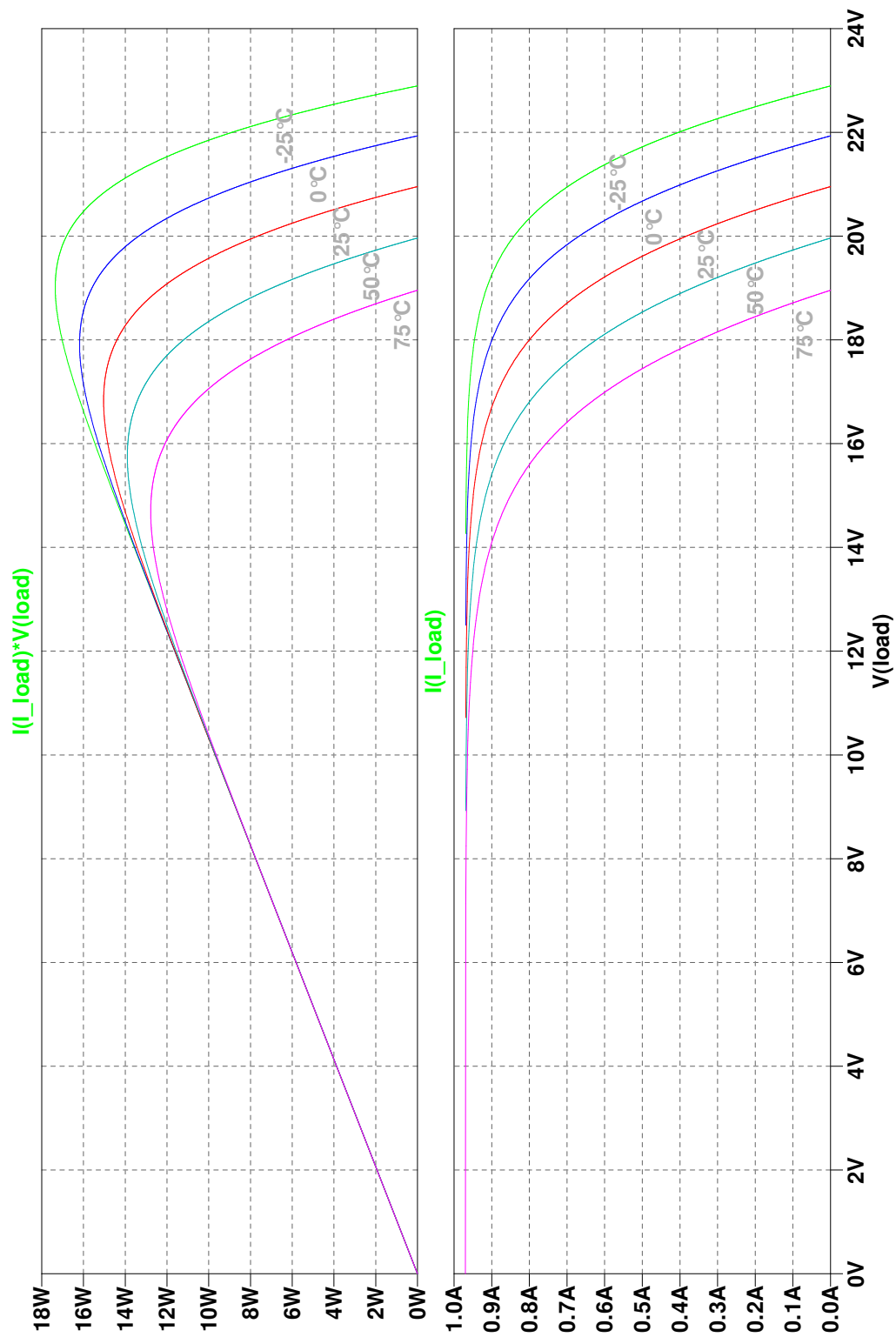


Figure 5.2: Simulation result of the used solar cell model. In the first graph one can obtain the output power whereas the second graph illustrates the U-I characteristics for a wide temperature range.

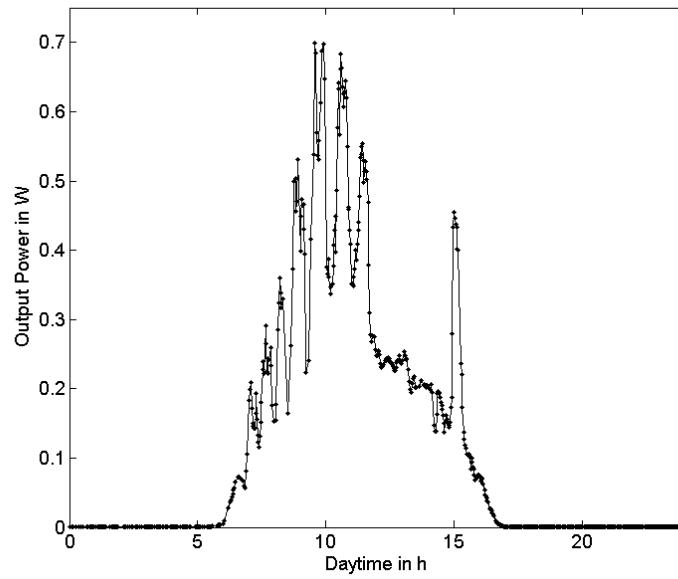


Figure 5.3: Output power measurement of a solar cell that had been placed on a north-facing balcony.

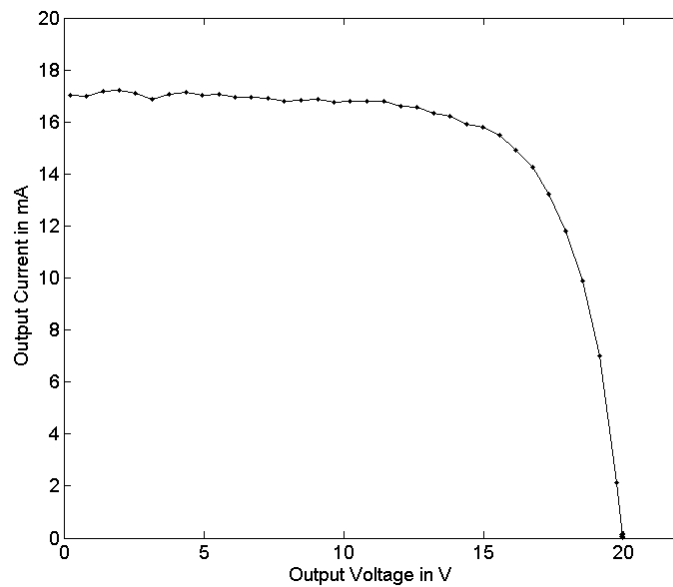


Figure 5.4: U-I characteristics of the used solar cell, located on a north-facing balcony.

5.2 Reverse Current Mode

The LM3488 is a current mode controller and therefore controls the current through the primary inductor. In 4.1.3 a power Mosfet has been selected, that is to say, the sense resistor has to be chosen very carefully. For this purpose the AN-1484 proposes

$$R_{sense} = \frac{V_{sense} - D \cdot (V_{SL} + \Delta V_{SL})}{I_{peak}} = \frac{V_{sense}}{I_{peak}} \approx 42 \text{ m}\Omega \quad (5.1)$$

whereas V_{sense} is 162 mV and $V_{SL} = 0$ V due to the non-existence of slope compensation. In the first tests one could observe that the power losses on the Mosfet were too high and also the temperature of the power Mosfet should not be too high in case of direct sunlight, so a higher R_{sense} of 50 m Ω could limit the switching current.

Due to the fact that the power Mosfet gets hot during operation, two tests have been carried out. First, a 25-minute permanent stress test with approximately 5-minute test intervals was applied. The second test dealt with the decrease in temperature over the time after the reverse current mode had been switched off. During the measurements, an infrared thermometer had been used to measure the temperature rise on the solar panel as well as the temperature of the MOSFet. The measured data is presented in Tables 5.1 to 5.2 and illustrated in Figures 5.5 to 5.6.

Table 5.1: Measurement of the temperature on the power Mosfet and the solar panel when driving system into reverse current mode.

Time [s]	Temp. on Solar cell [°C]	Temp. on Mosfet [°C]
0	22.4	22.6
30	22.8	30.6
60	23.0	34.0
120	23.4	38.0
300	25.0	45.4
600	26.4	47.2
900	27.0	49.2
1200	27.6	49.0
1500	28.4	49.6

Table 5.2: Measurement of the decrease in temperature on a solar panel and the power Mosfet after switching off the reverse current mode.

Time [s]	Temp. on solar cell [°C]	Temp. on Mosfet [°C]
0	28.4	49.6
30	28.2	40.4
90	28.0	36.4
150	27.6	33.8
300	27.0	29.6
600	25.2	26.0

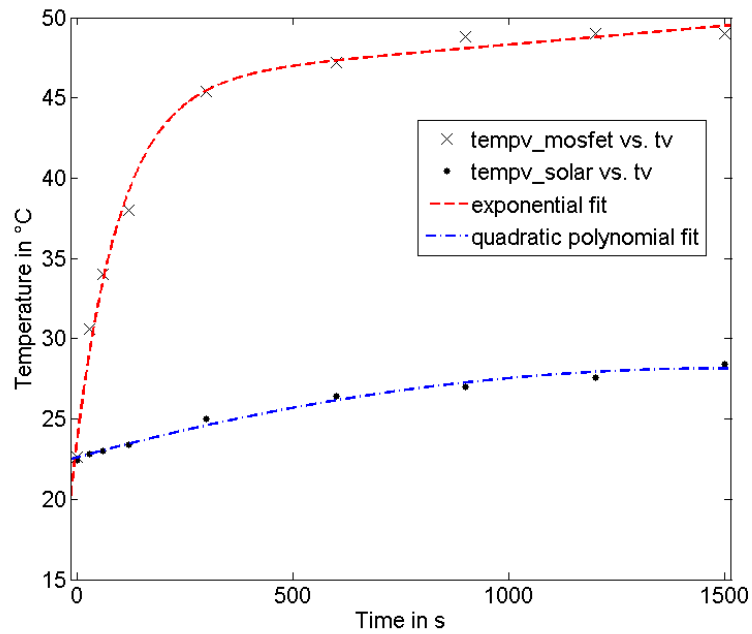


Figure 5.5: Temperature rise of the Mosfet and the solar panel during the stress test.

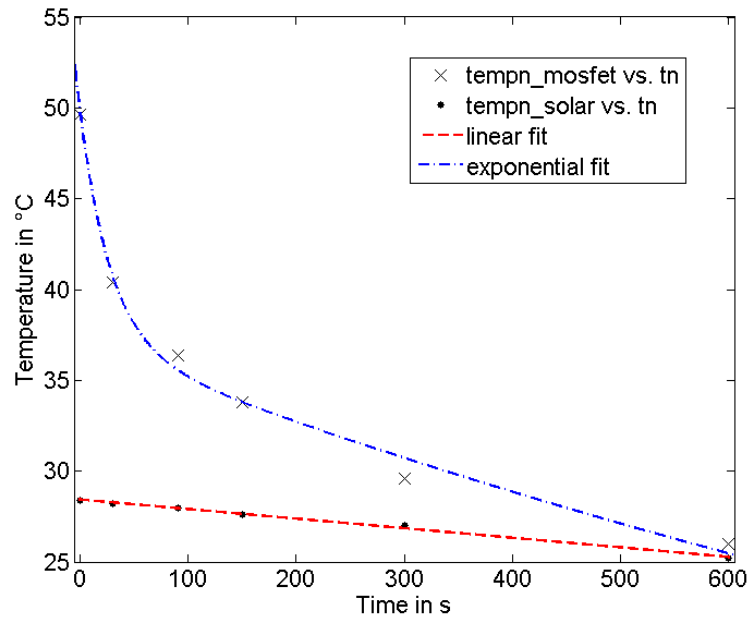


Figure 5.6: Temperature decrease of Mosfet and solar panel after switching off the reverse current mode.

5.3 Maximum Power Point Tracking

The simulation of the maximum power point tracker had been carried out in LTSpice. The solar cell is presented as a combination of a current source with diodes which had been shown in chapter 5.1. This model gives us an open circuit voltage of 21.2 V and a short circuit current of 970 mA. As SEPIC converter the LTC3786 controller had been chosen which is controlled via the LTC4000-1 that serves as the charging IC. The values of the components are chosen as calculated in chapter 4.

The battery is simulated with a combination of a voltage source and a capacitor in series. This model has been assumed of LT due to the problematic initial conditions. The complete model is shown in the appendix A.2 and the simulation results in Figure 5.7.

In Figure 5.7 a whole charging cycle is simulated at a temperature of 50 °C. Therefore it is assumed that the microcontroller has calculated the maximum power point and programmed a resistor size of 3180 Ω . The three plot planes describe the (i) switching behaviour of the charging IC, (ii) the current in the battery respectively the load and last (iii) the voltages at the input, load and battery.

The simulation starts with the enabling of reset#, so the charge# flag is set and the voltage on the IFB pin is tracked. At about 6 ms, when the voltage on the IFB pin is in steady state, the SEPIC converter starts to run and charges the battery.

As the battery voltage reaches 14.6 V and, therefore, charging finishes, the charge# flag goes up and the charging IC tells the SEPIC controller to slow down by reducing the voltage on the ITH pin. Now the SEPIC controller stresses the input less and the output voltage of 13.5 V, which is equal to the battery's floating voltage, is regulated.

5.3.1 Selection of an algorithm

Although the Maximum Power Point Algorithms are implemented, a comparative study which one is better or faster without a measurement hardware and an appropriate software is not possible. Nevertheless the algorithms had been tested and a maximum power point could be regulated.

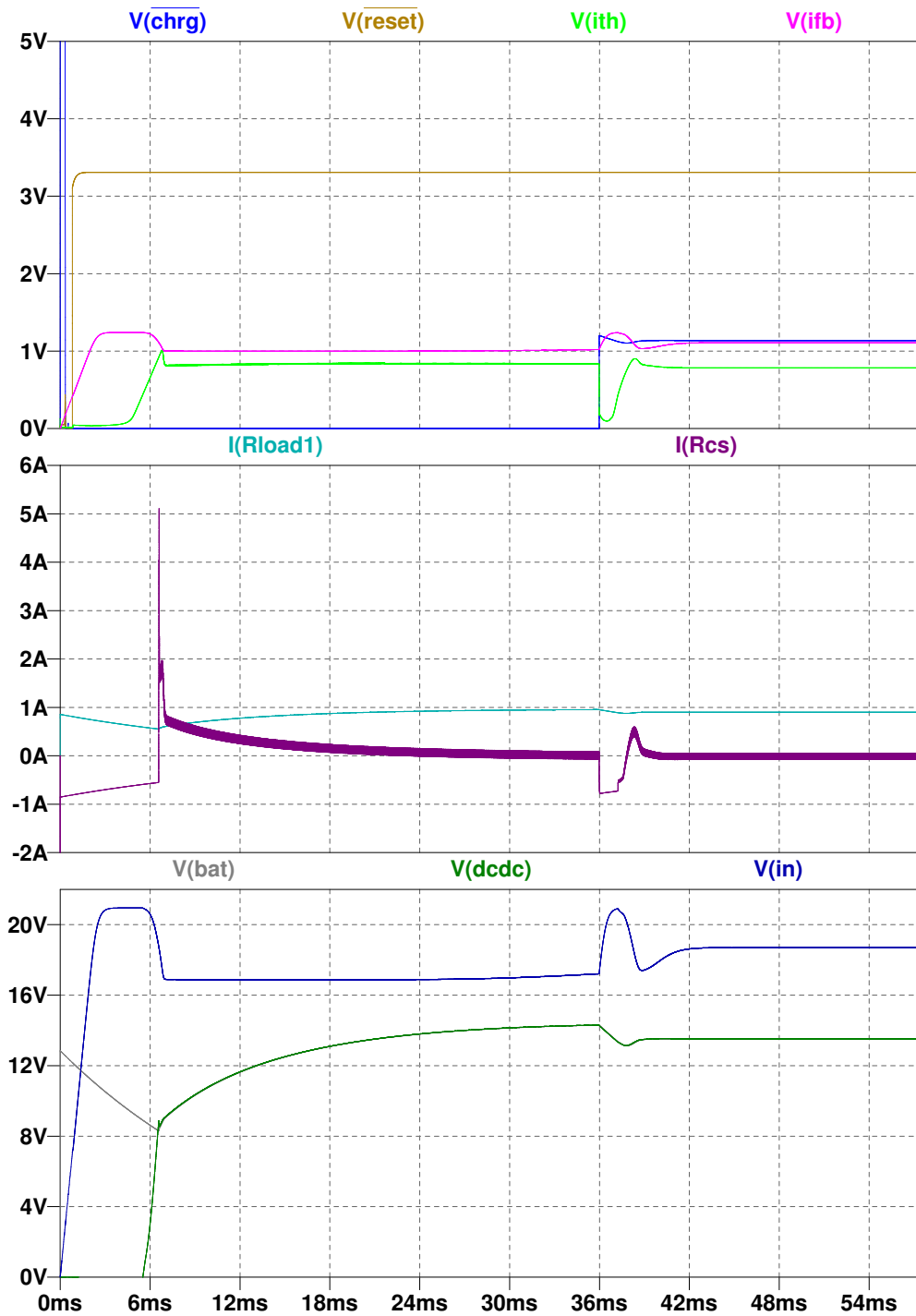


Figure 5.7: Simulation results for a whole charging cycle at a temperature of 50 °C.

Chapter 6

Conclusion and Outlook

Landslides are a common problem in Austria. For this purpose, a landslide early warning system has been developed. In this Master Thesis, an energy harvesting system has been presented which is capable of

- supplying a high power consuming sensor node
- de-icing a solar cell
- keeping the connected energy source at its maximum power point
- communicating with other different sensor nodes via I2C

Including GPS, GPRS and the sensor node, the EHS is mounted in a IP68 case with a clear front. This offers the possibility of placing a light intensity sensor inside the case for measurements. With the GPS position data, one can measure movement in all directions. Sensor data like temperature or air humidity values will allow a conclusion about the endangerment of the surveyed hillside.

6.1 System Overview

The system is comprised of four main parts. First, the energy sources like the solar cell as well as the lead acid battery, can be easily plugged in and form a continuous supply to the sensor node. Due to the high power consumption, a 20 Ah battery and a solar cell with a maximum power output of 15 W peak is needed. To keep the system at the maximum power point, the LTC4000-1 can manipulate the SEPIC converter with a compensation pin. For this purpose, the resistor divider of the input feedback loop of the LTC4000-1 is changed by a digital potentiometer. The calculation of the necessary resistor size can be done statically or dynamically with the Fractional Open Circuit Voltage or the Perturb and Observe algorithm.

The second part is the energy management and includes the charging of the lead acid battery. This is done with the LTC4000-1, which comes with the well-known charging algorithm for lead acid batteries. So the battery can be charged with a maximum current of 1.51 A.

The reverse current mode for de-icing a solar cell is the third component. This SEPIC

converter is capable of driving about 13 W at the output to de-ice the solar cell. The fourth and last part is the sensor node's supply, which is implemented with a high efficiency buck converter. This converter provides 3.4 V at a maximum output current of 500 mA.

6.2 Improvements

Although proper functionality with this design is given, a few improvements could be made. One problem that arose was controlling the MPP tracking algorithm. Due to the internal clock of 16 MHz and a PWM signal of 500 kHz, a maximum number of 32 cycles could be reached. So if one wanted to calculate more complex algorithms or adjust a few parameters according to temperature values, the 32 cycles are too few to respond. Using a DSP or a microcontroller with a faster external oscillator may be a good choice.

A few PCB EMC criteria like the placement of all connectors on one PCB side have been fulfilled, nevertheless, there are plenty of possibilities to further improve the EMC. PCB track loops which form antennas could unintentionally be created due to the problematic two layer PCB. More layers on the PCB could also greatly decrease the size of the board. Huge improvements can be made on the reverse current mode. Although the actual design works pretty well, it is possible to replace the existing design by a similar design which is used for the MPP tracker. The only real difference would be the switching frequency which should be significantly higher, ≈ 550 kHz. This would also make future orders much easier on Farnell, due to lower component counts. Furthermore, the coil and the MOSFET can become really hot, reaching about 50°C after 25 minutes of operation. The use of a DPAK transistor instead of the existing SOIC8 MOSFET and use of thermal vias can effectively reduce the temperature on the board.

While all of the resistor values are currently written over SPI, there is also the possibility to increment or decrement the value written in the potentiometer. This could lead to a three-wire SPI instead of four-wire.

In another project, a comparative design could be tested. In this case the GPS positioning with its complex algorithm could be replaced by a very simple sensor node with an accelerometer. An interrupt is driven when the hillside moves. This may not be the best design to supervise a hillside, but a very cheap method for monitoring avalanches by placing hundreds or even thousands of sensor nodes over a huge area.

Appendix A

Acronyms and Abbreviations

ADC	Analog to Digital Converter
AC	Alternating Current
COTS	Common Off-the-Shelf
DC	Direct Current
DSP	Digital Signal Processor
ECU	Electronic Control Unit
EHD	Energy Harvesting Device, e.g. Photovoltaic Cell
EHS	Energy Harvesting System
I2C	Serial Interface
ICs	Integrated Circuits
IR	International Rectifier, a manufacturer of power semiconductors
LDO	Low Dropout Regulator
LTC	Linear Technology Corporation
MCU	Microcontroller Unit
MOSFET	Metal Oxide Semiconductor Field Effect Transistor
MPP	Maximum Power Point
MPPT	Maximum Power Point Tracking
PCB	Printed Circuit Board
PWM	Pulse Width Modulation
RAM	Random Access Memory

SMD	Surface Mounted Device
SoC	State of Charge (Battery)
SPI	Serial Peripheral Interface, a duplex high-speed serial interface
TI	Texas Instruments
WSN	Wireless Sensor Network

A.1 Functional Block Diagram LTC4000-1

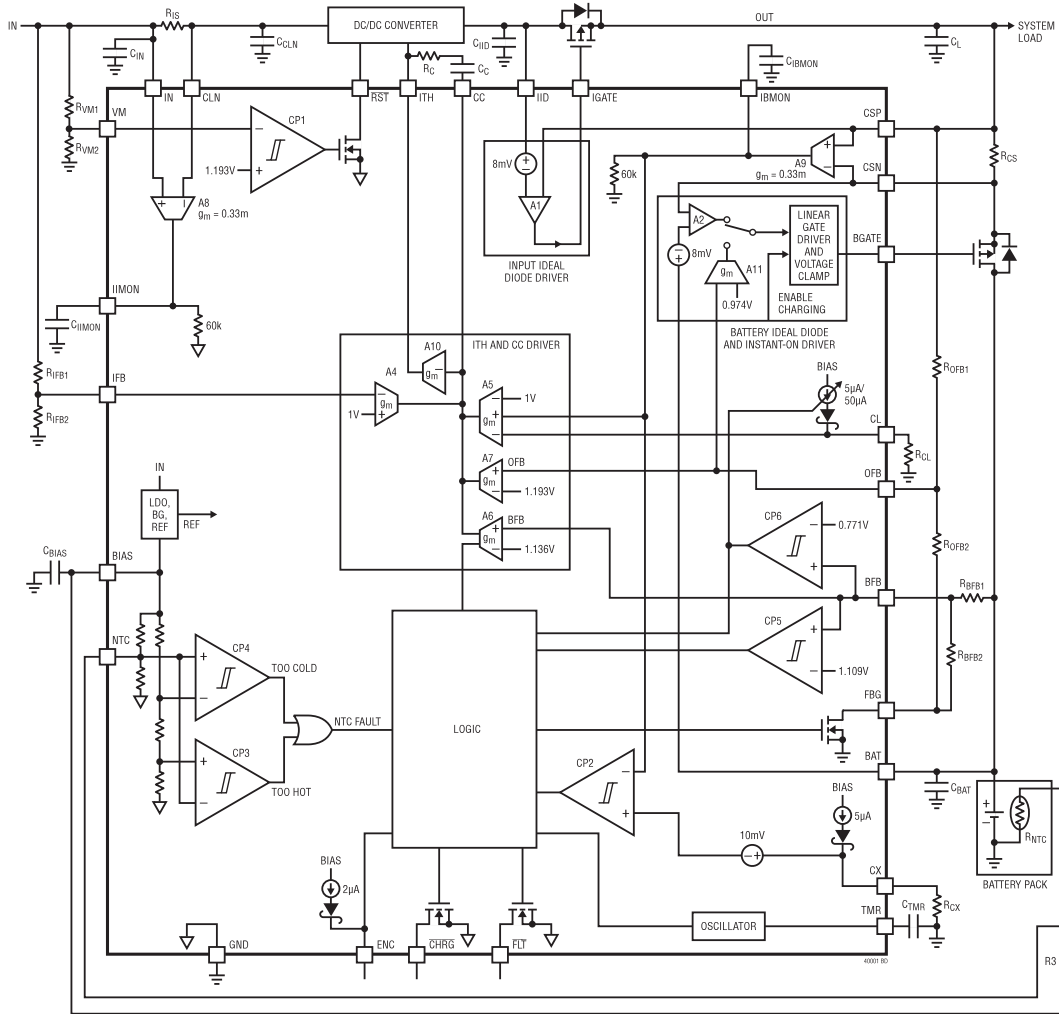
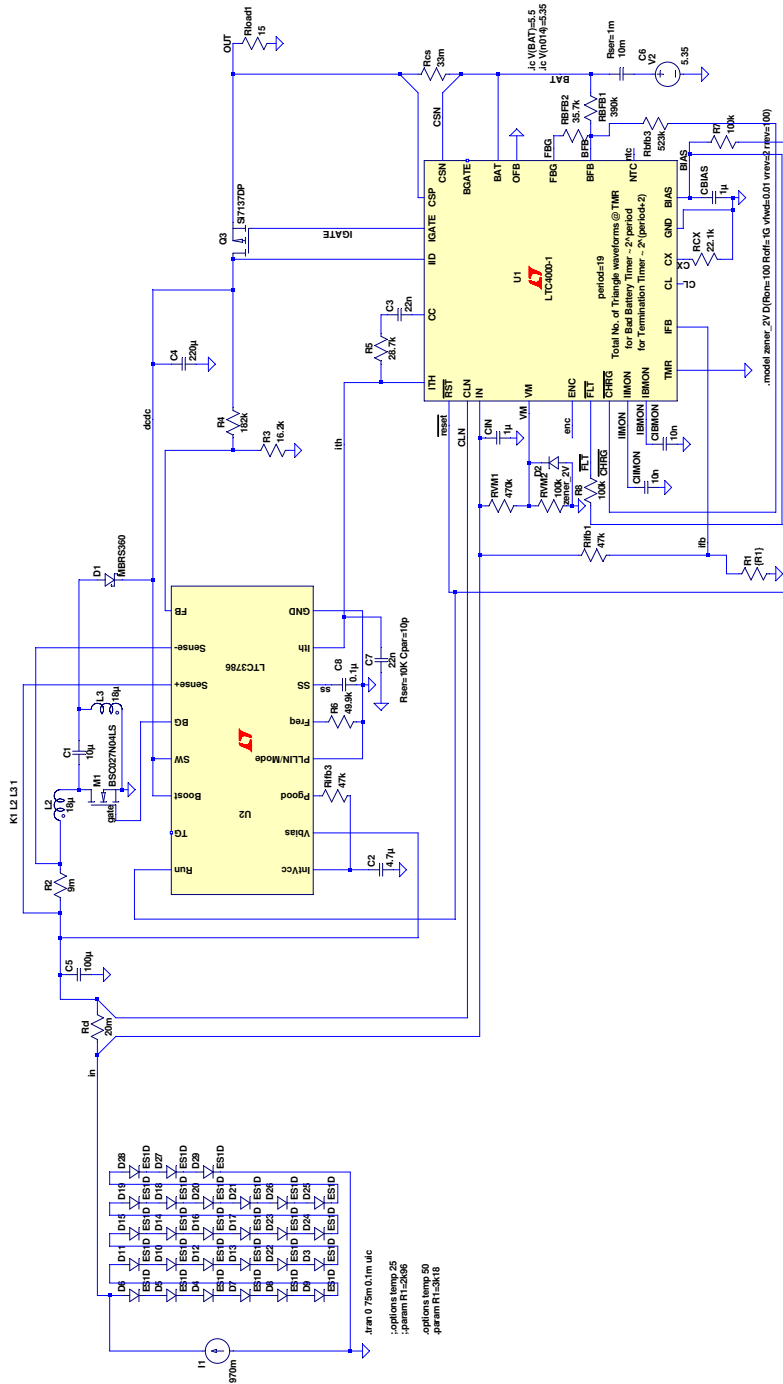


Figure A.1: Block diagram of the LTC4000-1 charging IC, [37]

A.2 Simulation Model of the MPP Tracker



Appendix B

Schematics and Layout

The schematics and the layout of the energy harvesting system are presented in the following four figures. The first three figures deal with the schematics, whereas only the last figure shows the layout which had been created in Eagle. Figure B.1 illustrates the power converter which supplies the load with 3.4V and a maximum current of 500mA, as well as the integration of the current shunt monitor with protection against common-mode transients.

Figure B.2 contains the implementation of the maximum power point tracker and the charging IC. It is also shown how to plug in the battery.

The last schematic figure B.3 refers to the integration of the MSP430F2274 and the SEPIC converter which will control the reverse current mode. The layout will conclude the design process and areas of components are marked on the board.

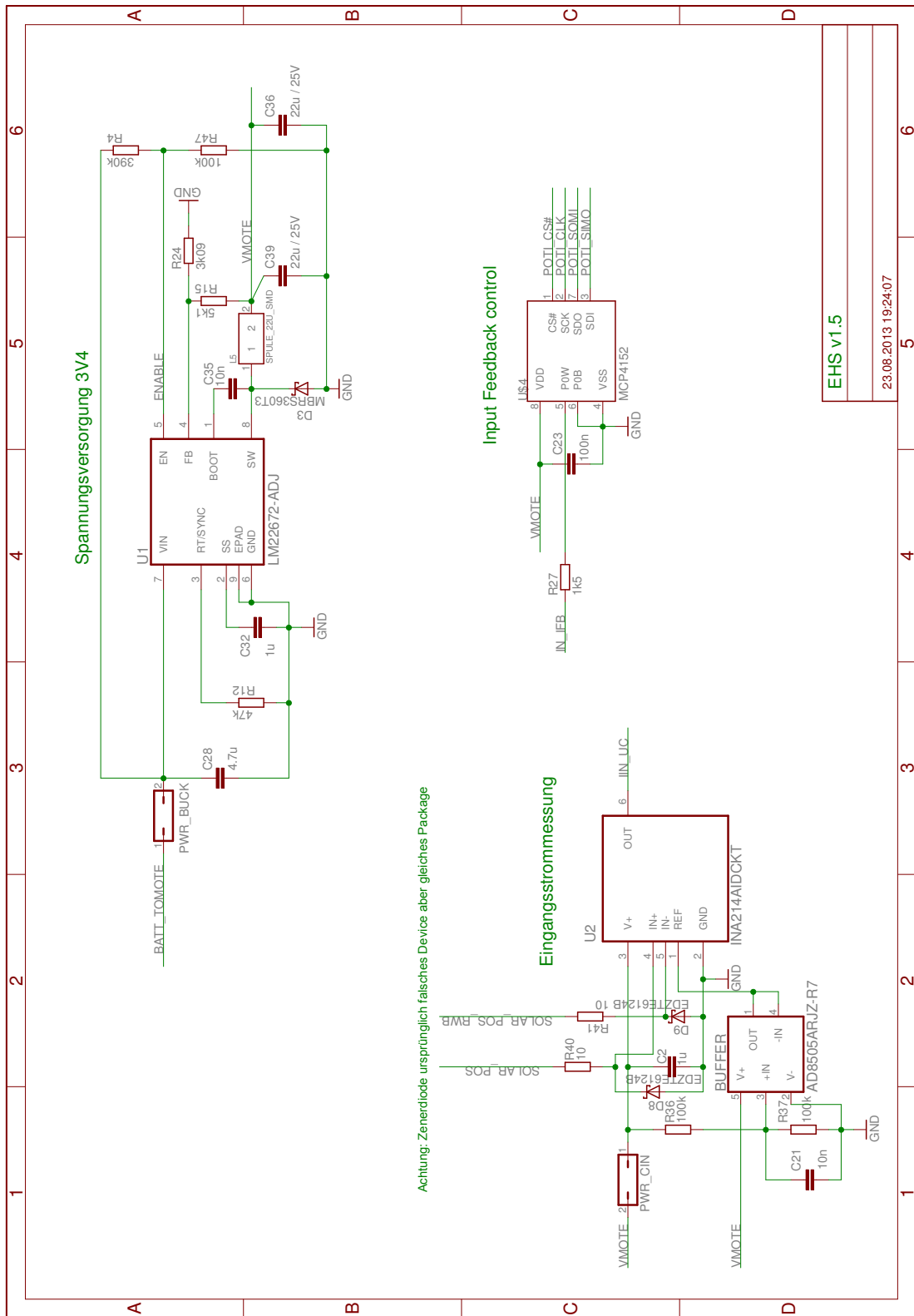


Figure B.1: Schematics of the Energy Harvesting System (1/3)

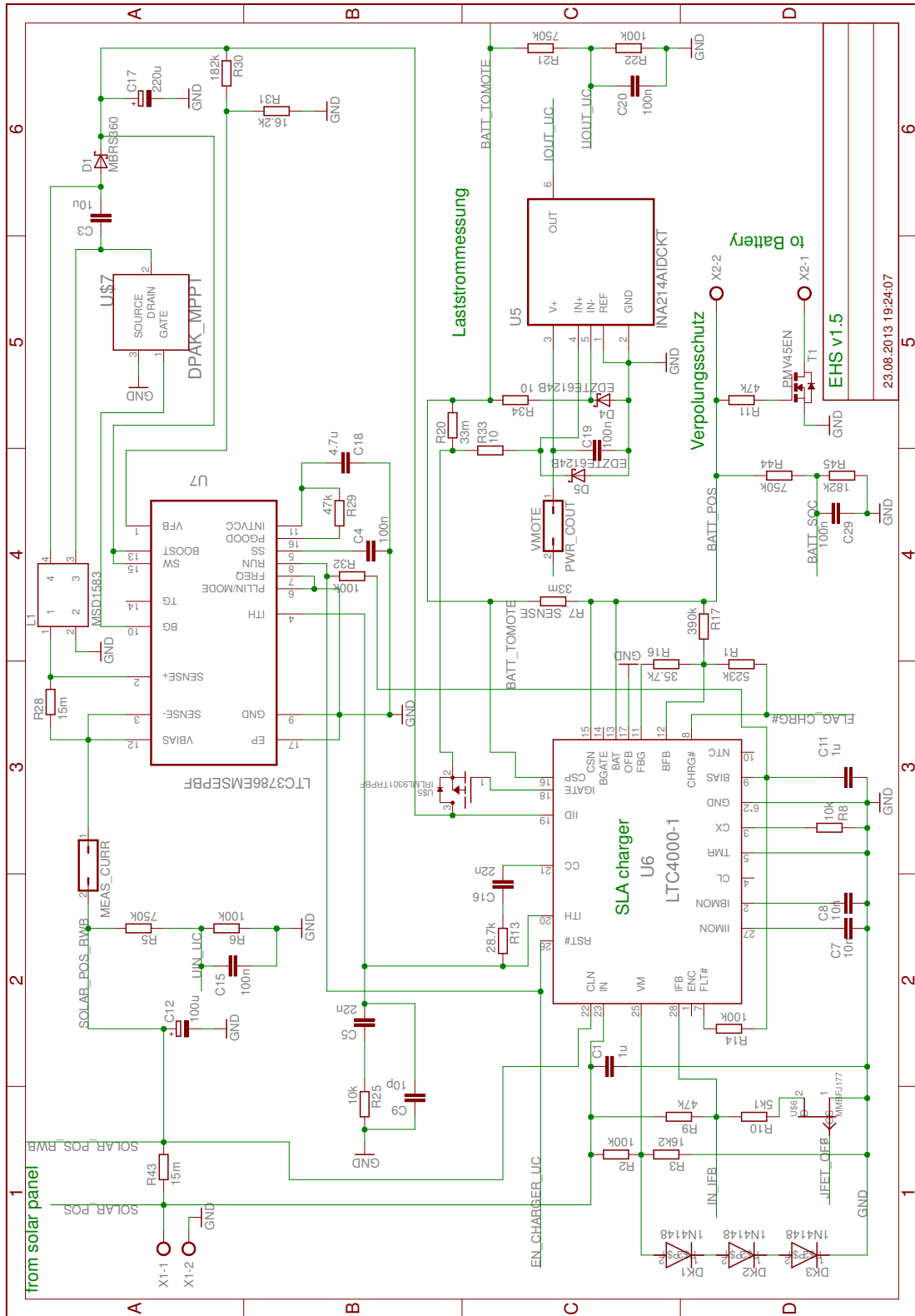


Figure B.2: Schematics of the Energy Harvesting System (2/3)

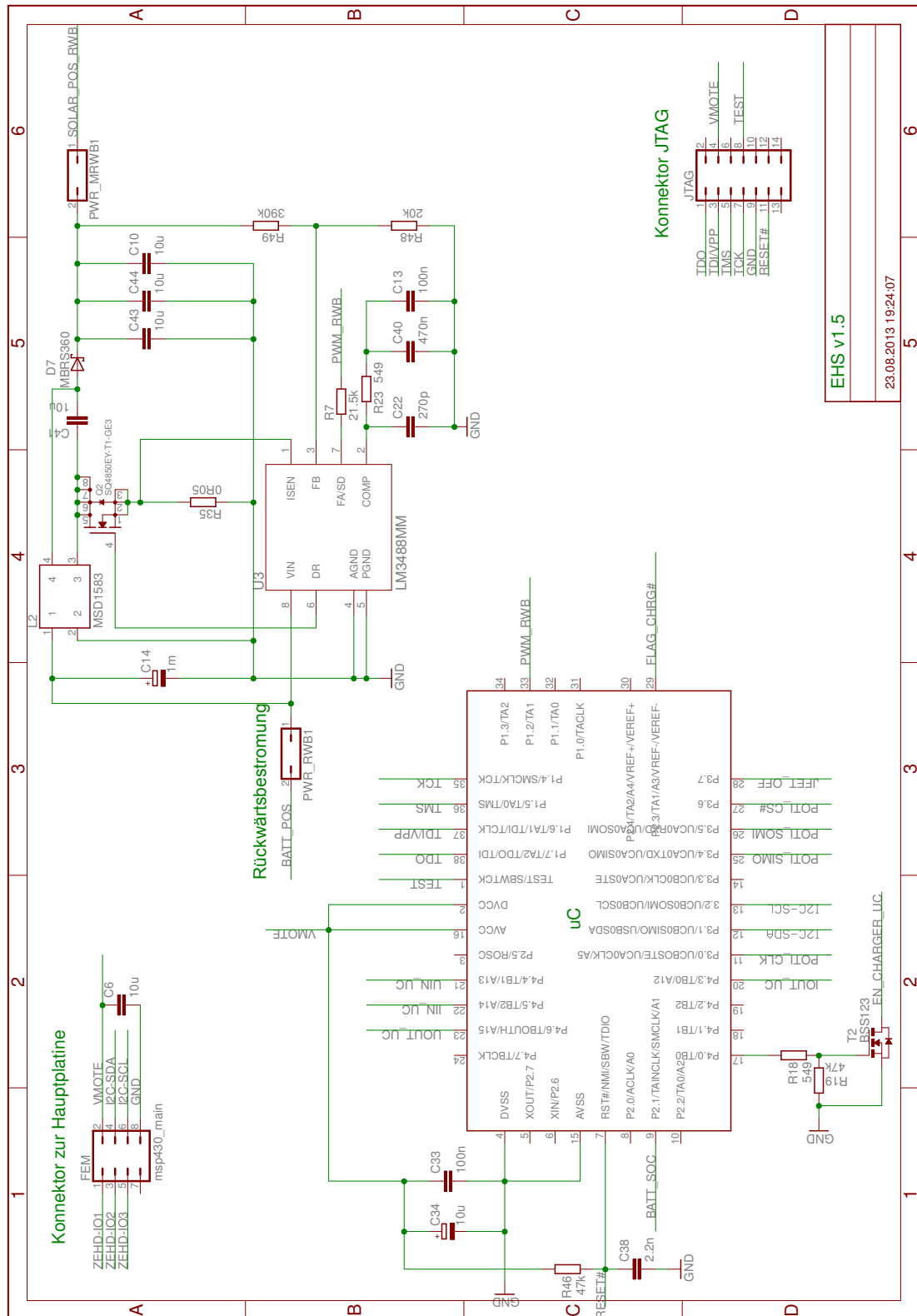


Figure B.3: Schematics of the Energy Harvesting System (3/3)

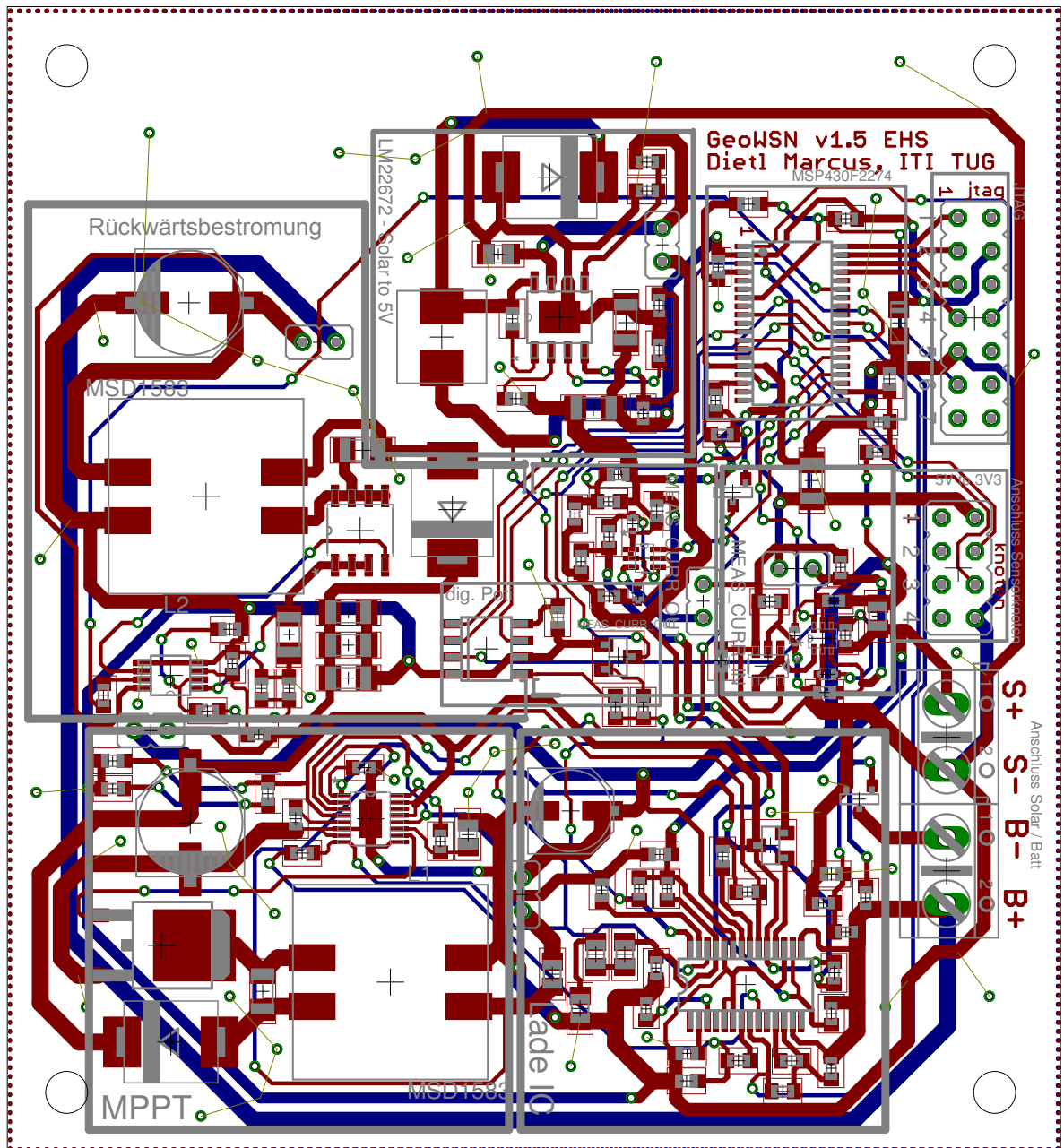


Figure B.4: Layout of the Energy Harvesting System

Bibliography

- [1] Jawad Ahmad, *A Fractional Open Circuit Voltage Based Maximum Power Point Tracker for Photovoltaic Arrays*, 2nd International Conference on Software Technology and Engineering (ICSTE), 2010
- [2] D. Dondi, A. Batacchini, L. Larcher, P. Pavan, D. Brunelli, L. Benini, *A Solar Energy Harvesting Circuit for Low Power Applications*, IEEE International Conference on Sustainable Energy Technologies, 2008
- [3] Pan Lei, Gong Wei, Wang Yinghong, *Maximum Power Point Tracking Control of Solar Photovoltaic Power Generation System Based on Model Reference Adaptive*, IEEE International Conference on Sustainable Power Generation and Supply, 2009
- [4] D. P. Hohm, M. E. Ropp, *Comparative Study of Maximum Power Point Tracking Algorithms Using an Experimental, Programmable, Maximum Power Point Tracking Test Bed*, IEEE Conference Record of the Twenty-Eighth Photovoltaic Specialists Conference, 2000
- [5] K.H. Hussein, I. Muta, I. Hoshino, M. Osakada, *Maximum photovoltaic power tracking: an algorithm for rapidly changing atmospheric conditions*, IEEE Proceedings-Generation, Transmission and Distribution Volume 142, Issue 1, 2002
- [6] David Salerno, *Ultralow Voltage Energy Harvester Uses Thermoelectric Generator for Battery-Free Wireless Sensors*, LT Journal of Analog Innovation Volume 20 Number 3, October 2010
- [7] Tellurex Corporation, *Frequently Asked Questions About Our Power Generation Technology*, technology review, 2013
- [8] Academic dictionaries and encyclopedias, *Gleichspannungswandler*, <http://de.academic.ru/dic.nsf/dewiki/>, 30.01.2013
- [9] Jose Formenti and Robert Martinez, *Design Trade-offs for Switch-Mode Battery Chargers*, Texas Instruments Portable Power Design Seminar, 2004
- [10] Texas Instruments, *AN-1484: Designing a SEPIC converter*, SNVA168D revised version April 2008
- [11] Kristaps Vitolis, Nadav Reinberg, Alvis Sokolovs, Ilya Galkin, *Drive Selection for Electric Kart*, 14th International Power Electronics and Motion Control Conference, 2010

- [12] Costis Kompis, Simon Aliwell, *Energy Harvesting Technologies to Enable Remote and Wireless Sensing*, Sensors and Instrumentation: Knowledge Transfer Network, June 2008
- [13] Photovoltaik Austria, *Sonnenscheindauer und Globalstrahlung*, <http://www.pvaustria.at/>, 22.11.2012
- [14] T. Sogorb, J.V. Llario, J. Pelegri, R. Lajara, J. Alberola, *Studying the Feasibility of Energy Harvesting from Broadcast RF Station for WSN*, IEEE Instrumentation and Measurement Technology Conference Proceedings, 2008
- [15] Ing. Davide Brunelli, *Wireless Sensor Networks*, Università di Bologna, 2008
- [16] Marcus Dietl, *Entwurf und Implementierung der Hardware-Architektur eines drahtlosen Sensorknotens zur Überwachung gefährdeter Hänge mittels GPS*, Masterprojekt, 2013
- [17] Online Compendium, Isidor Buchmann, *The Battery University*, <http://batteryuniversity.com/>, 11.12.2012
- [18] Shad Roundy, Dan Steingar, Luc Frechette, Paul Wright, and Jan Rabaey, *Power Sources for Wireless Sensor Networks*, Kapitel 3.1 Electromagnetic (RF) Power Distribution
- [19] Chulsung Park and Pai H. Chou, *AmbiMax: Autonomous Energy Harvesting Platform for Multi-Supply Wireless Sensor Nodes*, 3rd Annual IEEE Communications Society on Sensor and Ad Hoc Communications and Networks, 2006. SECON
- [20] D. Meckhun, V. Boitier and J. M. Dilhac, *Design of a Solar Harvester System for a Wireless Sensor Network Deployed for Large Aircraft In-Flight Tests*, International Conference on Renewable Energies and Power Quality 2012
- [21] Farhan Simjee and Pai H. Chou, *Everlast: Longlife, Supercapacitor-operated Wireless Sensor Node*, International Symposium on Low Power Electronics and Design (ISLPED) 2006
- [22] Michal Kocglán, Peter Sevcik, *Supercapacitor power unit for an event-driven wireless sensor node*, IEEE Proceedings of the Federated Conference on Computer Science and Information Systems pp. 791-796, 2012
- [23] Chulsung Park, Kanishka Lahiri and Anand Raghunathan, *Battery Discharge Characteristics of Wireless Sensor Nodes: An Experimental Analysis*, In Proceedings of the IEEE Conf. on Sensor and Ad-hoc Communications and Networks (SECON), 2005
- [24] J.F. Christmann, E. Beigné, C. Condemine and J. Willemin, *An Innovative and Efficient Energy Harvesting Platform Architecture for Autonomous Microsystems*, 8th IEEE International NEWCAS Conference, 2010
- [25] Satish Mohanram, *Developments in Energy Harvesting for WSN*, www.electronicmaker.com/, 23.04.2013

- [26] Günther Lemmerer, *Laden von Calcium/Calcium Batterien*, <http://www.bannerbatterien.com/banner/infocenter/index21.php>, 21.02.2013
- [27] Andreas Wagner, *Photovoltaik Engineering: Die Methode der effektiven Solarzellen-Kennlinie*, Auszug aus Kapitel 2, erschienen 1999 im Springer Verlag Berlin Heidelberg
- [28] Florent Boico and Brad Lehman, *Study of Different Implementation Approaches for a Maximum Power Point Tracker*, Northeastern University, 2006 IEEE COMPEL Workshop
- [29] Norbert Graubner, *SMD-Reflow-Löten für Amateure*, <http://www.beta-store.com/rkde/index.html>, 13.05.2013, Funkamateureur 12/09
- [30] PCB Pool, *Strombelastbarkeit von Kupfer (CU)-Leiterbahnen*, CM-SO-001/A/2009 C
- [31] Paul Rudelstorfer, *Evaluation of thermic based energy harvesting for wireless sensor networks*, to be published
- [32] Coilcraft, *Selecting coupled inductors for SEPIC applications*, Document 639-1, Revised 01/28/2008
- [33] Michael Steinberger, *Automatische Charakterisierung von Energiegewinnungskomponenten*, Masterprojekt, November 2012
- [34] Stephan Gether, *Design and Implementation of a distributed wireless sensor node software for a slope movement monitoring system*, Master Thesis, Institute for Technical Informatics TU Graz
- [35] Texas Instruments, *Benefits of a coupled-inductor SEPIC converter*, Analog Applications Journal, 2Q 2011
- [36] Texas Instruments, *Coupled inductors broaden DC/DC converter usage*, Analog Applications Journal, 3Q 2010
- [37] Linear Technologies, *High Voltage High Current Controller for Battery Charging with Maximum Power Point Control*, Datasheet of LTC4000-1, page 12, 10.07.2013